Review

Energy Storage Materials

B. Mendoza-Sánchez,* Y. Gogotsi*

.....x–xx

Synthesis of Two-Dimensional Materials for Capacitive Energy Storage

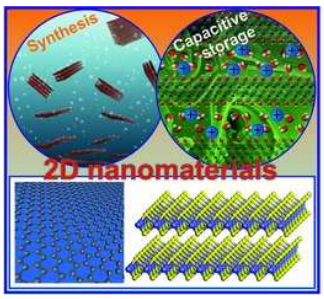

Advances in the synthesis and applications of 2D nanomaterials for capacitive energy storage are reviewed. Graphene, transition metal oxides, dichalcogenides and carbides that are being explored for capacitive energy storage are described, and key factors that influence their performance are analyzed. Challenges and opportunities in synthesis, electrochemical stability, electrode design and architecture are thoroughly discussed and future research opportunities are outlined.

adma201506133(201506133)

www.advmat.de ADVANCED MATERIALS

Synthesis of Two-Dimensional Materials for Capacitive Energy Storage

By *Beatriz Mendoza-Sánchez* and Yury Gogotsi**

Keywords: 2D materials, electrode architecture, hierarchical structure, hybrid devices, supercapacitors

ABSTRACT: The unique properties and great variety of two-dimensional (2D) nanomaterials make them highly attractive for energy storage applications. Here, we provide an insight into the progress made towards the application of 2D nanomaterials for capacitive energy storage. Synthesis methods and electrochemical performance of various classes of 2D nanomaterials, particularly based on graphene, transition metal oxides, dichalcogenides and carbides, are presented. The factors that directly influence capacitive performance are discussed throughout the text and include nanosheet composition, morphology and texture, electrode architecture and device configuration. Recent progress in the fabrication of 2D nanomaterials based microsupercapacitors and flexible and free-standing supercapacitors is presented. Main electrode manufacturing techniques with emphasis on scalability and cost-effectiveness are discussed and include laser scribing, printing, and roll-to-roll manufacture. Various issues that prevent the use of the full energy storage potential of 2D nanomaterials and how they have been tackled are discussed and include nanosheets aggregation and low electrical conductivity of some 2D nanomaterials. Particularly the design of hybrid and hierarchical 2D and 3D structures based on 2D nanomaterials is presented. Other challenges and opportunities are discussed and include: control of nanosheets size and thickness, chemical and electrochemical instability, and scale-up of electrode films.

1. Introduction

2D nanomaterials are single- or few-atom thick crystals with the term "nano" referring to their ultrathin thickness.[1] They can also be referred to as "nanosheets".[2] Because of an intrinsically high specific surface area of atomically thin sheets, 2D nanomaterials are attractive for capacitive energy storage.[3] Various 2D nanomaterials have been investigated for this application and include graphene,[4] transition metal oxides,[1,2,5] transition metal dichalcogenides,[2,6] and transition metal carbides and nitrides (MXenes).[7–11]

Electrochemical capacitors or supercapacitors store energy by two mechanisms: electrical double layer capacitance (EDLC) and pseudocapacitance.[12] Electrical double layer capacitance originates from the formation of an electrical double layer upon device polarization. The ions of the electrolyte adsorb onto the electrode surface of opposite charge leading to charge separation at the electrode-electrolyte interface in a rapid (seconds) and reversible manner.[12] The electrical double layer capacitance is defined as

$$C = \varepsilon_r \varepsilon_0 \frac{A}{d}, \quad (1)$$

where ε_r is the relative permittivity of the electrolyte, ε_0 is the permittivity of vacuum, A is the electrode surface area and d is the thickness of the electrical double layer. Pseudocapacitance involves a rapid (within a second or less) and reversible transfer of Faradaic charge at the electrode-electrolyte interface.[12] This charge transfer can involve oxidation-reduction (redox) processes and/or ion intercalation processes, but not phase transformations.[12] The gravimetric energy density of a supercapacitor is defined as

$$E = \tfrac{1}{2}\frac{CV^2}{m}, \quad (2)$$

where C is capacitance, V is the voltage window and m is mass. Volumetric energy density is expressed as

$$E_V = \tfrac{1}{2}\frac{CV^2}{Vol}, \quad (3)$$

B. Mendoza-Sánchez, Laboratory of Physical Chemistry of Materials and Electrolytes for Energy Applications, University François Rabelais of Tours, Tours, 37200, France
Y. Gogotsi, A. J. Drexel Nanotechnology Institute, and Department of Materials Science and Engineering, Drexel University, Philadelphia, PA, 19104, USA
Correspondence to: B. Mendoza-Sánchez (E-mail: beatriz.mendoza@univ-tours.fr), Y. Gogotsi (E-mail: yg36@drexel.edu)
10.1002/adma.201506133

where *Vol* is volume.

2D nanomaterials have a high specific surface area suitable for high double layer capacitance (**Equation** (1)). Inorganic 2D nanomaterials have reactive basal planes and edges that can provide pseudocapacitance. They can be modified by chemical functionalization and doping to provide additional reactive sites. This is the case also for reduced graphene oxide (rGO) that holds oxygen-containing chemical functionalities. 2D nanomaterials have the ability to intercalate ions and thus can provide intercalation pseudocapacitance. Moreover, 2D nanomaterials can store energy in the 2D channels between nanosheets by a fast ion adsorption mechanism enabled by the pre-intercalation of water molecules and a rapid expansion and contraction of the multi-layered and flexible 2D nanomaterials.[13] Unlike rigid porous 3D materials, such as hard carbons undergoing slow diffusion processes, the nature of 2D nanomaterials favors a fast ionic transport through 2D channels that are free to expand and contract.

Due to their subnanometer thickness, 2D nanomaterials have a high packing density that leads to a high volumetric capacitance, which is important for manufacturing thin-film supercapacitors. The flexibility of 2D nanomaterials, good mechanical properties, and high packing densities make them suitable for the development of thin, flexible and all-solid state supercapacitors and microsupercapacitors.[5,14]

Energy storage requires a suitable electrical conductivity that is fulfilled by some 2D nanomaterials in their natural state such as the zero band gap semiconductor graphene,[15,16] some metallic MXenes[17] and 1T transition metal dichalcogenides[18] which have been used to manufacture electrodes free of electrically conducting additives. However, most 2D nanomaterials do not have sufficient electrical conductivity and this hampers their application in energy storage.[6] The electronic structure of 2D nanomaterials is directly influenced by their number of atomic layers and crystal structure.[6,19] Methods to alter the electronic structure of 2D nanomaterials to enhance electrical conductivity have been devised and include surface modification by chemical functionalization, intralayer doping and lattice strain.[20] Conversely, the natural electrical conductivity of some 2D nanomaterials, such as graphene, can be undermined by chemical functionalization and introduction of porosity.

One of the main challenges to exploit the full potential of 2D materials to store energy is to prevent nanosheet re-stacking that prevents full utilization of surface area and blocks electrolyte access (**Figure 1a**). This problem has been tackled by tailoring nanosheet morphology. Synthesis methods have been developed to produce nanosheets in shapes other than flat. Curved or crumpled nanosheets generate porosity when deposited onto current collectors facilitating ion transport (**Figure 1b**).[21] Nanosheets can also be grown directly in a vertical orientation onto current collectors leaving suitable channels for ion transport (**Figure 1c**).[22] Various synthesis methods have been applied to graphene to introduce porosity on the nanosheets, which facilitates ion transport across nanosheets (**Figure 1d**).[23,24]

2D nanomaterials can be used as building blocks for a variety of hybrid and hierarchical 2D and 3D structures,[25] such as aerogels that in turn serve as scaffolds for other nanomaterials

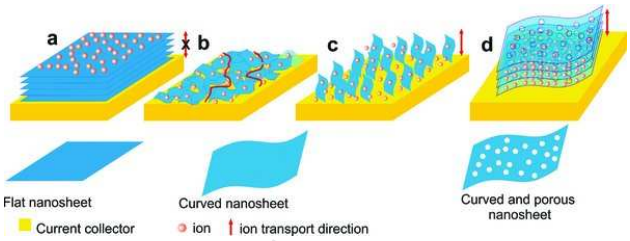

Figure 1. Schematic describing the role of 2D nanomaterial shape and morphology on ion transport properties in energy storage devices: a) ion transport hindered by flat and stacked nanosheets, (b) curved nanosheets deposited onto current collector with suitable porosity for ion transport, (c) vertically grown nanosheets onto current collector enabling ion transport through nanosheet-nanosheet spaces, and (d) stacked but porous and curved nanosheets that allow ion transport through pores and across nanosheets. Q4

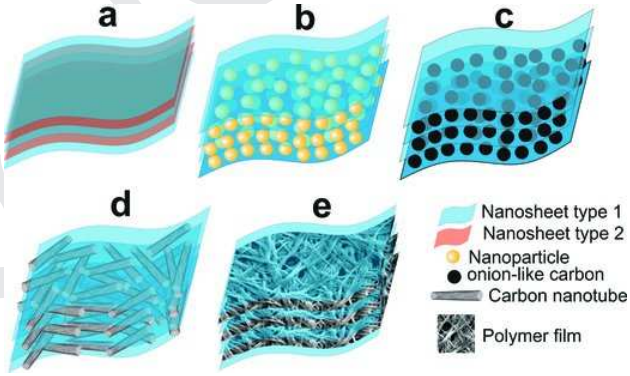

Figure 2. Schematics of hybrid structures comprised of (a) two types of interleaved nanosheets and inserted (b) nanoparticles, (c) onion-like carbon, (d) carbon nanotubes, and (e) polymer films into nanosheet-nanosheet spaces. Q5

such as nanoparticles.[26] This versatility offers the possibility to engineer superstructures tailored for a great variety of applications, including energy storage. Semiconducting or insulating 2D nanomaterials, such as metal oxides, can be combined with electrically conductive ones, such as graphene, in a 2D hybrid (**Figure 2**a) to enhance energy storage properties.[27,28] A strategy to overcome re-stacking is the intercalation of large molecules or incorporation of nanoparticles[29] (Figure 2b**)** such as onion-like carbon (OLC)[30] (Figure 2c), carbon nanotubes[30] (Figure 2d) and polymers (Figure 2e).[31,32]

In this article we provide an overview of the applications of 2D nanomaterials in supercapacitors. Synthesis methods are mentioned briefly and the focus is kept on capacitive energy storage related properties and performance - for a general description of mechanical, electronic and optical properties and a more general overview of energy storage and conversion applications that include devices other than supercapacitors, the reader is referred to recently published reviews.[33] First, capacitive properties of various 2D nanomaterials such as graphene, metal oxides, transition metal chalcogenides and MXenes are

Beatriz Mendoza Sánchez received a B.Eng. (Hons) degree in Chemical Engineering from University of Guanajuato, Mexico (2002), a M.Sc. degree in Nanoscale Science and Technology from Chalmers University of Technology, Sweden (2006) and a D.Phil. in Materials Science from University of Oxford, UK (2012). Her PhD research targeted applications of graphene and nanostructured metal oxides for thin film supercapacitors manufactured by spray-deposition. Her current research interests include two-dimensional and hybrid materials for thin film energy storage devices, the development of Na-ion batteries based on layered metal oxides, and the study of electrode-electrolyte interfaces and energy storage mechanisms.

Yury Gogotsi is Distinguished University Professor and Trustee Chair of Materials Science and Engineering at Drexel University in Philadelphia, USA. He is the founding Director of the A.J. Drexel Nanomaterials Institute. He works on nanostructured carbons and two-dimensional carbides for energy related and biomedical applications. He has co-authored 2 books, more than 400 journal papers and obtained more than 50 patents.

Q6

described. Next, important aspects of material morphology and design, electrode architecture, device configuration, and manufacturing techniques are discussed. Finally, challenges and opportunities in the application of 2D nanomaterials for supercapacitors are discussed.

2. Classes of 2D Nanomaterials for Capacitive Energy Storage

Various 2D nanomaterials have been investigated to date for capacitive applications. Here, we make distinction of classes of 2D nanomaterials based on the type of capacitive energy storage mechanism and nature of the 2D nanomaterial. First, we consider graphene and graphene-based materials that store energy mainly using a double layer charge storage mechanism but also pseudocapacitive mechanisms, when doped or chemically functionalized. The first subsection describes details of the adopted nomenclature. The topic is then divided into subsections that classify the graphene-based materials according to nanosheet morphology, concentration of basal-plane defects, electrode design and architecture, and chemical functionalization. In addition, new studies revealing the role of quantum capacitance and subnanometer 2D nanochannels on energy storage of graphene-based materials are reviewed. Next, inorganic 2D nanomaterials with redox and ion intercalation pseudocapacitive properties are considered, which include 2D metal oxides, transition metal dichalcogenides, and transition metal carbides. Emphasis is placed on intrinsic physical and chemical properties that directly affect capacitive energy storage ability and that are often determined and controlled by material synthesis methods.

2.1. Graphene

The high theoretical surface area of graphene of 2,630 $m^2\ g^{-1}$ and its exceptional electronic properties,[16,34] make it appealing for energy storage applications. Since the works of C.N.R. Rao[35] and R.S. Ruoff[4] published in 2008, an intensive research activity seeking to apply graphene in supercapacitors has resulted in various findings regarding chemical properties (presence or not of chemical functionalities on the basal plane and/or edges), the texture (structural defects or pores, size of pores), morphology and orientation of the graphene layers that favors one or another energy storage process.

Graphene has been synthesized using a variety of methods including chemical vapor deposition (CVD), physical or chemical exfoliation, and reduction of graphite oxide. The reader is referred to comprehensive reviews dedicated to graphene synthesis.[36,37]

It is opportune to mention some facts about the properties of graphene: (1) upon contact with each other, graphene layers have a natural tendency to restack due to $\pi-\pi$ interactions, (2) the electronic properties of graphene are compromised if the carbon lattice with sp^2 configuration is disrupted and (3) graphene's properties are a function of the number of constituent layers.

2.1.1. Graphene Definition and Nomenclature

Graphene is defined as an infinite 2D (one atom thick) crystal constituted by sp^2-hybridized carbon atoms arranged in a hexagonal lattice.[38,39] The two-dimensionality of graphene is determined by freestanding single layers. Crystals containing two or more layers are considered pseudo-2D systems as their electronic properties are different than those of graphene (2D) and graphite (3D).[39] In the literature, the name graphene has been used for a variety of materials that do not fulfill the above definition of graphene. Recently, the editorial published in *Carbon* has recommended a systematic nomenclature for the family of "graphene materials",[40] which will be adopted in this article. Wherever possible we make distinctions between: (1) graphene, as defined above, (2) few-layer (FL) graphene (2-5 layers), (3) multilayer (ML) graphene (2-10 layers), (4) graphene oxide (GO), a chemically modified graphene prepared by oxidation and exfoliation that is accompanied by extensive oxidative modification of the basal plane, (5) reduced graphene oxide (rGO), a GO that has been reductively processed by chemical, thermal, microwave, photo-chemical, or photo-thermal methods to reduce its oxygen content,[40] and (6) graphite, considered a 3D crystal made of graphene layers (>10).[15,37,39]

2.1.2. Graphene with a Low Content of Lattice Defects

ADVANCED MATERIALS www.advmat.de

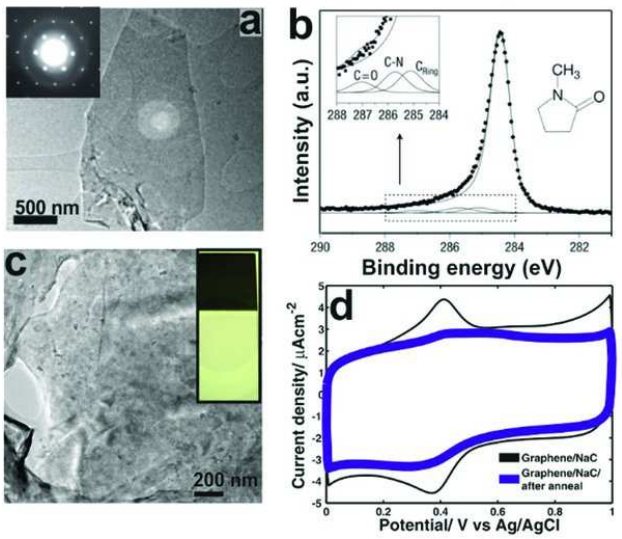

Figure 3. Graphene produced by liquid-phase exfoliation and its supercapacitor performance.[42,43] a) Transmission electron microscopy (TEM) image (scale bar 500 nm) and diffraction pattern of SL-graphene produced by liquid-phase exfoliation in NMP,[42] (b) a carbon 1s core-level XPS spectrum showing absence of oxygen-containing chemical functionalities other than those attributed to residual NMP. c) TEM image of a spray-deposited film of graphene obtained by liquid-phase exfoliation in an aqueous/sodium cholate (surfactant) media and an optical image of a spray-deposited electrode on an ITO-coated glass substrate, and (d) corresponding cyclic voltammograms (at 50 mV s^{-1} in a 1 M H_2SO_4 electrolyte). The cyclic voltammograms correspond to electrodes tested before (black line) and after (blue line) annealing in inert atmosphere that removed the surfactant causing pseudocapacitive peaks. a–b) Reproduced with permission.[42] Copyright 2008, Nature Publishing Group. c–d) Reproduced with permission.[43] Copyright 2013, Elsevier.

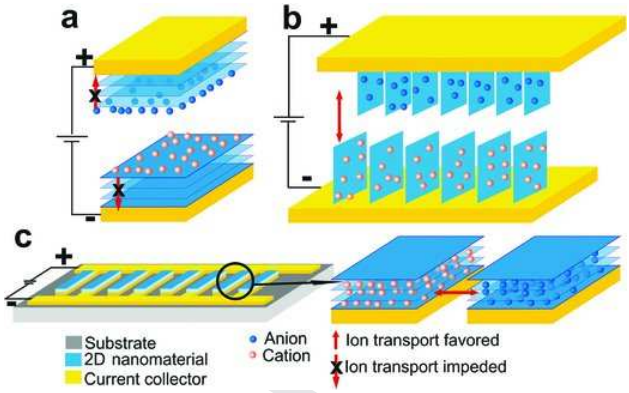

Figure 4. Schemes of supercapacitor configurations. a) "Sandwich" configuration and electrodes with stacked nanosheets or "out-of-plane" geometry (ion transport "out" of the basal plane of the nanosheet), (b) "sandwich" configuration and electrodes with vertically aligned nanosheets or "in-plane" geometry (ion transport "in-plane" with the basal plane of the nanosheet),[45] (c) interdigitated configuration with "in-plane" electrodes (in-plane with the current collector) made of stacked nanosheets.

Graphene Produced by Liquid-phase Exfoliation and Electrodes with an Out-of-plane Geometry Electrodes with a fast capacitive response but low capacitance have been produced by a combination of liquid-phase exfoliation and spray-deposition. Supercapacitor technology demands scalable methods to produce electrochemically active materials. Liquid-phase exfoliation is a method that produces mostly FL-graphene and its scalability has been recently demonstrated.[41,42] This method utilizes the energy produced by ultrasonic waves to separate the graphene layers of graphite immersed in a solvent, where the role of the solvent is to provide a suitable surface energy necessary to exfoliate graphite and prevent post-exfoliation aggregation. SL- but mostly FL-graphene has been produced by liquid-phase exfoliation in N-methyl-2-pyrrolidone (NMP).[42] A SL-graphene layer is shown in **Figure 3**a.

NMP-exfoliated graphene had a low degree of basal plane defects, as demonstrated by Raman spectroscopy and X-ray photoelectron spectroscopy (XPS) (Figure 3b) and a high electrical conductivity of ≈6,500 S m^{-1}.[42] A similar procedure uses water instead of organic solvents where surfactants are used to stabilize graphene against re-aggregation.[44] FL-graphene has been produced in this manner and utilized to produce thin-film (350 nm) supercapacitor electrodes using a spray deposition method (Figure 3c) and tested in a 1 M H_2SO_4 electrolyte.[43] The electrodes had an out-of-plane geometry, i.e., stacked graphene nanosheets onto current collectors, as described in **Figure 4**a and Section 3.1.

The graphene electrodes showed double layer capacitance and pseudocapacitance (Figure 3d); the latter attributed to the presence of surfactant residues. The electrodes had a low capacitance of 543 μF cm^{-2} and 12 F g^{-1}, and a fast response of 2.3 ms.[43]As shown in Figure 3d, upon annealing the surfactant was removed and the pseudocapacitive activity vanished. The low capacitance was attributed to re-stacking of the FL-graphene units upon removal of the carrier liquid during spray-deposition (scheme in Figure 1a) and the presence of a surfactant. Both conditions prevented adequate electrolyte access causing poor electrochemical utilization of the active material. The rapid capacitive response was attributed to the low concentration of defects (chemical functionalities and lattice defects) in the FL-graphene, as demonstrated by Raman spectroscopy ($I_D/I_G = 0.34$) and XPS, favoring a high electrical conductivity (4,900 S m^{-1}).[43] Similar testing was carried out using NMP-exfoliated FL-graphene, which also showed a low gravimetric and areal capacitance. The main drawback of liquid-phase exfoliation methods is a low yield combined with the high boiling point, toxicity, and corrosiveness of solvents such as NMP, which makes processability difficult. Aqueous exfoliation is a more environmentally friendly alternative, but the use of surfactants results in further electrode processing steps and may affect conductivity and performance of the electrodes.

CVD Graphene and Electrodes with an In-Plane Geometry Graphene for ultra-fast supercapacitors has been vertically

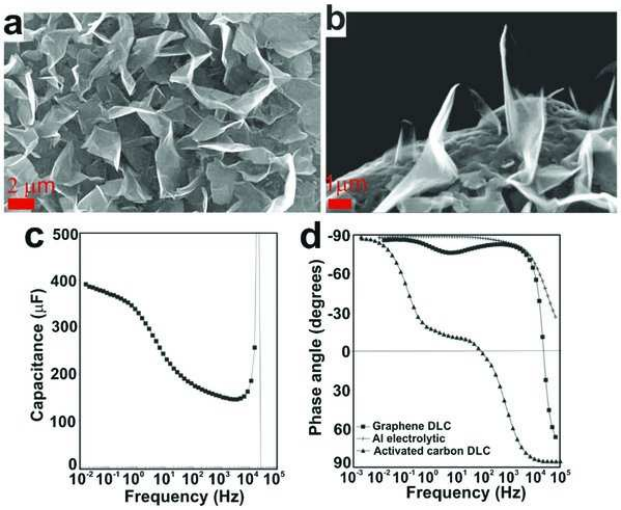

Figure 5. Graphene grown by a PECVD method and its supercapacitor performance.[22] SEM images of PECVD-grown graphene on (a) a nickel substrate and (b) a fiber; (c) capacitance vs frequency curve of a capacitor manufactured with PECVD-grown graphene and fitting to an RC circuit model; (d) impedance phase angle vs frequency curve (showing also the behavior of an Al electrolytic capacitor and an activated carbon-based capacitor). Reproduced with permission.[22] Copyright 2010, AAAS.

grown onto Ni substrates using plasma-enhanced chemical vapor deposition (PECVD) (**Figure 5**a-b).[22] The length of the graphene nanosheets was 600 nm and the thickness was reported to be < 1 nm (FL-graphene). The ending of each nanosheet was reported to be SL-graphene. Graphene grown by CVD methods has a low degree of lattice defects evidenced by Raman spectroscopy ($I_D/I_G = 0.67$) and therefore preserves a high electrical conductivity.[22] A symmetric device of 4 cm^2 geometric areashowed a low areal capacitance (Figure 5c) of 390 μF/4 cm^2 = 97.5 μF cm^{-2} but a fast capacitor response of 8.3 ms corresponding to an impedance phase angle of -83° at a frequency of 120 Hz (**Figure 5d**) in a KOH/water electrolyte. This last property was found suitable for AC-line filtering applications. The fast capacitance response was attributed to: (i) the architecture of the electrode having graphene nanosheets vertically aligned with respect to the current collector (Figures 5a-5b), i.e., in an in-plane geometry as described in Figure 4b and Section 3.1, (ii) the graphene nanosheets being well separated from each other, and (iii) the graphene edges being exposed to the electrolyte. These conditions favored a facile access of electrolyte ions minimizing ionic resistance. A direct attachment of the graphene to the metal current collector secured adequate electron transport minimizing electrical resistance.

It has been previously demonstrated with pyrolytic graphite that electrodes having an in-plane geometry (Figure 4b) with their edges preferentially exposed to the electrolyte, provide more capacitance (50-70 μF cm^{-2}) than electrodes with an out-of-plane geometry (3 μF cm^{-2}) (Figure 4a).[46,47] The capacitance of the device with an in-plane geometry produced by PECVD (390 μF cm^{-2} per single electrode)[22] was indeed larger than the capacitance of the electrodes with an out-of-plane geometry produced by liquid-phase exfoliation described above (221 μF cm^{-2}, 12 F g^{-1}).[43] However, neither material/electrode architecture is suitable for applications requiring high energy densities. In the former case, a low number of graphene layers per unit area results in a low gravimetric capacitance, especially when the total weight of the device is considered. In the latter case, the capacitance is clearly undermined by the graphene stacking phenomenon and decreases quickly with increasing electrode thickness. In other studies, electrodes with in-plane geometry were tested with solid state electrolytes showing geometric capacitances of 80 μF cm^{-2} for CVD grown SL-graphene and 390 μF cm^{-2} for ML-graphene derived from GO.[45]

2.1.3. Texture and Morphology Modifications of Graphene-based Materials

A popular method used to produce graphene-based materials for supercapacitors is based on the use of GO and subsequent reduction. This methodology introduced the concept of modified pristine graphene where: (i) lattice defects are first introduced by chemical oxidation of graphite, and then partial lattice restoration is sought by chemical or physical reduction, (ii) porosity is introduced on the basal planes of the graphene and (iii) mesoporosity of the electrode is induced by changing the nanosheet morphology. These modifications of the pristine graphene overcame the limitations imposed by the graphene stacking phenomenon and lead to improved energy and power density performance.

Chemically Reduced Graphene Oxide and Microwave-exfoliated Graphite Oxide Chemically reduced GO (CRGO) is typically produced as follows: GO is synthesized using established methods, then exfoliated in water and subsequently reduced by a chemical agent.[48,49] GO holds a series of chemical functionalities containing oxygen such as carbonyl, carboxyl, epoxide, and hydroxyl groups on basal planes and edges that disturb the sp^2 carbon bonding of the graphene backbone.[50] The reduction step seeks to remove those chemical functionalities to restore the graphene lattice but usually some chemical functionalities and structural defects remain. **Figure 6**a–b shows CRGO that consisted of 15–20 μm nanoparticles with a degree of aggregation and a reported electrical conductivity of 200 S m^{-1} and a capacitance of 100 F g^{-1} in a TEA BF_4/acetonitrile (MeCN) electrolyte.[49] The agglomeration of this material occurred during the reduction in solution, and/or solvent removal. An alternative method to overcome this problem was the use of microwaves[51] to reduce and exfoliate GO producing expanded micro-wave exfoliated graphite oxide (MEGO), with a specific surface area of 463 m^2 g^{-1} (Figure 6c).[52] Figure 6d shows a C_{1s} core level XPS spectrum of MEGO that shows evidence of the presence of oxygen-containing chemical functionalities. Notice the difference with respect to the equivalent spectrum of liquid-phase exfoliated graphene shown in Figure 3b. A symmetric supercapacitor showed a capacitance of 191 F g^{-1} in a 5 M KOH electrolyte and a 1 V electrochemical window (Figure 6e).[52] Other methods to reduce GO include the use of hy-

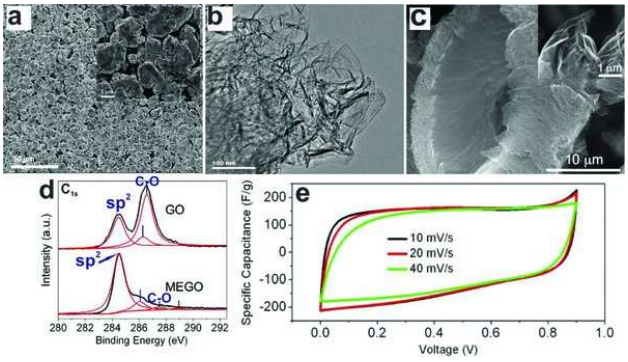

Figure 6. a–b) CRGO,[49] c–e) MEGO[52] and their supercapacitor performance. a) Scanning electron microscopy (SEM) images of CRGO particles, (b) TEM image of rGO sheets protruding from a CRGO particle, (c) SEM image of MEGO showing its crumpled morphology, (d) a carbon 1s core-level XPS spectrum of GO and MEGO where C-O indicates chemical functionalities containing oxygen (hydroxyl, carboxyl, epoxide, etc. groups), (e) cyclic voltammograms of a MEGO supercapacitor tested in 5 M KOH electrolyte. a–b) Reproduced with permission.[49] Copyright 2008, American Chemical Society. c–e) Reproduced with permission.[52] Copyright 2010, Elsevier.

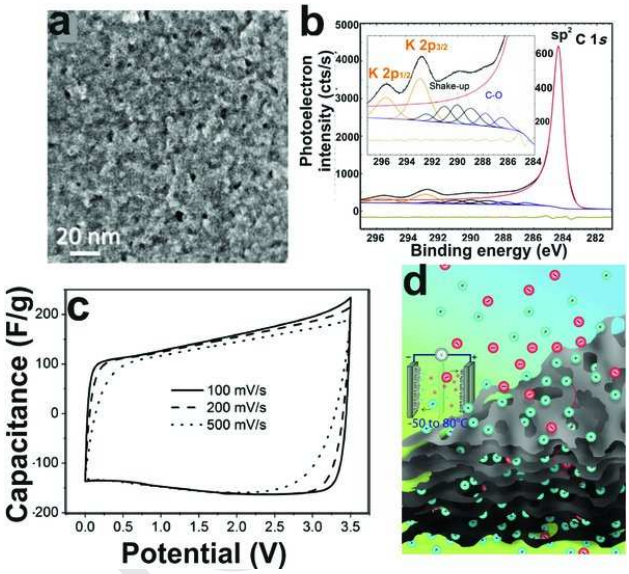

Figure 7. a-MEGO and its supercapacitor performance.[23] a) High resolution SEM image of a-MEGO where porosity of 2–10 nm can be observed, (b) a carbon 1s core-level XPS spectrum of a-MEGO showing components corresponding to C-O bonds, shake up peaks and K_{2p} levels core levels corresponding to impurities, (c) a cyclic voltammogram of a symmetric supercapacitor tested in a BMIM BF_4/MeCN electrolyte, and (d) a schematic of a supercapacitor showing the ion transport across micro-and meso-porous nanosheets. a–c) Reproduced with permission.[23] Copyright, 2011 AAAS. d) Reproduced with permission.[57] Copyright 2015, The Authors.

drazine gas[53] or temperature to produce thermally exfoliated graphite oxide (TEGO) with a specific surface area of 368 m^2 g^{-1}, a capacitance of 264 F g^{-1} in a 5.5 M KOH electrolyte and 122 F g^{-1} in [$MeEt_3N$]BF_4/MeCN electrolyte.[54]

The important contribution of these studies is that they provided evidence of the large influence of chemical functionalities, nanosheet morphology and surface area exposed to the electrolyte on capacitance. CRGO had larger capacitances than FL-graphene produced by liquid-phase exfoliation described above. A main advantage of CRGO over rigid carbons, as described by the authors, is that the transport of ions is easier through flexible graphene layers than through rigid pores.[4,48]On the other hand, due to the presence of lattice defects, rGO has a lower electrical conductivity than FL-graphene produced by other methods such as the chemical vapor deposition (CVD) and liquid-phase exfoliation. Consequently, the power density of rGO is inferior to that of FL-graphene with substantially lower degree of lattice defects. This drawback has been alleviated by the activation of rGO as described next.

GO-based Materials Incorporating Porosity In a further step, R.S. Ruoff and co-workers produced a KOH-activated graphene that incorporated micro- and mesoporosity.[23] As the authors called it, "a-MEGO" was prepared by microwave exfoliation of graphite oxide, followed by impregnation with KOH and heat treatment in argon at 800° C. The following properties of a-MEGO were reported: (i) predominately SL-graphene, (ii) incorporated pores of 1–10 nm responsible for (**Figure 7**a) (iii) a specific surface area of ≈3,000 m^2 g^{-1}, (iv) 98 % sp^2 bonding, (v) a C/O atomic ratio of 35, and (vi) a powder electrical conductivity of 500 S m^{-1}. Raman studies showed I_D/I_G ratios of 1.16 and 1.19 for MEGO and a-MEGO, respectively. This shows a larger degree of defects than for liquid-phase exfoliated ($I_D/I_G = 0.34$) and PECVD grown graphene ($I_D/I_G = 0.67$). Figure 7b shows the C_{1s} core level XPS spectrum of a-MEGO showing evidence of a minor content of oxygen-containing chemical functionalities. A symmetric device of this material was reported to have capacitances of 166 F g^{-1} and ≈60 F cm^{-3} in a 1-butyl-3-methylimidazolium-tetrafluoroborate (BMIM BF_4)/MeCN electrolyte in a working electrochemical window of 3.5 V. A cyclic voltammogram is shown in Figure 7c. A maximum energy density of 70 Wh kg^{-1} and power density of 250 kW kg^{-1} were reported. Self-standing electrodes were also produced by a slightly modified procedure using GO without microwave treatment followed by a similar activation process.[55] This material was reported to have an electrical conductivity of up to 5,800 S m^{-1}. In combination with a mixed ionic liquid electrolyte, a-MEGO electrode can operate from −50°C to 80°C, achieving 150 F g^{-1} at room temperature and operating in a 3.5 V window.[56] An alternative method to produce microporous graphene uses ultrasonication of GO in an oxidizing acid such as HNO_3.[24]

The high power density performance of the a-MEGO deserves further discussion. The microporosity of carbons (pore size <2 nm) was traditionally associated with a loss of capacitance at high current densities, i.e., decreasing power density due to slow transport of ions in micropores. On the other hand, a carbon texture with a reduced concentration of lattice defects

and all storage on the outer surface is associated with a large electrical conductivity and a high power performance, but low capacitance, as previously demonstrated for carbon onions.[58] In the case of a-MEGO a high power density was facilitated by: (i) fast transport of ions that simply jump into mesopores and across graphene layers, as shown in Figure 7d,[57]] rather than diffusing through an intricate network of micropores with narrow bottlenecks which are typical of activated or carbide-derived carbons,[[59,60] (ii) a suitable electrical conductivity (500 S m^{-1}) due to a largely preserved sp^2 bonding configuration,[55] and (iii) good interparticle connectivity. The large energy density (Equation (2)) of a-MEGO can be attributed to a combination of the enhanced and accessible surface area (Figure 7d) introduced by the activation process that generated micro- and mesopores, and the use of an electrolyte that operates in a wide voltage window.

2.1.4. Graphene Doping and 3D Graphene Architectures

Nitrogen Doping Doping of graphene is a method to add pseudocapacitive properties to double layer capacitive graphene-based materials. Substitution of the carbon atoms in the graphene lattice with heteroatoms gives rise to a material with different electronic properties and surface chemistry. Doping of graphene with nitrogen transforms graphene[15] to an n-type semiconductor.[61,62] In the context of supercapacitors, the presence of heteroatoms on the graphene surface provides pseudocapacitive activity, but the disruption of the graphene lattice undermines the electrical conductivity. Carrier mobility decreases from 300–1200 cm^2 V^{-1} s^{-1} for pristine graphene to 200–450 cm^2 V^{-1} s^{-1} for nitrogen doped graphene.[61] Graphene has been doped with nitrogen using two kinds of methods: (i) post-synthetic methods that include plasma treatment of GO[63,64] or CVD-grown graphene,[65] chemical[66] and hydrothermal treatment of GO,[67,68] and (ii) in situ methods that include CVD[61,62] and pyrolysis.[69] The materials obtained by these methods had a varying degree of nitrogen incorporation (up to 10 %), number of graphene layers, topological defects and overall texture and morphology. A nitrogen doped rGO with a "crumpled" morphology has been produced by reaction of GO with cyanamide, followed by thermal treatment.[66] The material had a capacitance of 284 F g^{-1} in a 1 M $[Bu_4N]BF_4$/MeCN electrolyte, four times larger than the capacitance of non-doped and similarly produced material.[66] A good rate capability was shown for this material with a capacitance of 226 F g^{-1} at 10 A g^{-1}. The enhanced capacitance was attributed to a larger pore volume generated by the crumpled morphology and microporosity. A similar material consisting of crumpled nitrogen-doped graphene was synthesized by thermal expansion of GO followed by hydrothermal treatment with hexamethylenetetramine and had a capacitance of 270 F g^{-1} in 1 M H_2SO_4.[67] The role of the thermal treatment was key to avoid aggregation and increase surface area. Electrodes of nitrogen-doped graphene synthesized by an ammonia plasma treatment of GO and manufactured by spray-deposition had a "flat" morphology and a capacitance of 9.5 mF cm^{-2} in 1 M H_2SO_4 in a half-cell configuration.[63] This capacitance was 10 times larger than the capacitance of non-functionalized graphene.[43]

The increase of capacitance of nitrogen-doped graphene is a function of the uniformity of the doping and whether it is in one or both sides of the graphene layers. Doping not only affects the electronic structure and properties of graphene, but it also reduces the degree of aggregation and results in a morphology that allows easy access of electrolyte ions. Recent findings show that a larger capacitance of nitrogen-doped a-MEGO as compared to non-doped a-MEGO may be correlated to an increase of quantum capacitance of nitrogen-doped graphene-like micropore walls (see Section 2.1.5). Microporosity enhances surface area, but may have a detrimental effect on power density. In the case of rGO, its incomplete reduction leaves oxygen-containing chemical functionalities that contribute to pseudocapacitance in aqueous electrolytes. As outlined in the following section, doping with elements other than nitrogen has been achieved in combination with a highly porous aerogel structure.

Aerogels and Hydrogels of Doped rGO Graphene-based aerogels are 3D architectures made of rGO units that are suitable for developing binder-free, all-solid-state supercapacitors. The key advantage of graphene-based aerogels compared to activated carbons is that they can be compressed without fracture. Their 3D porous architecture offers a high-surface-area-to-volume ratio ideal for infiltration of solid or gel electrolytes. The assembly of graphene into a 3D structure has been achieved by a combination of sol–gel synthesis techniques and hydrothermal treatment or pyrolysis. A typical procedure involves the suspension of GO in water, followed by the addition of a chemically reducing agent to the mix and a hydrothermal treatment to form a hydrogel. The hydrogel is subsequently dried using supercritical fluids or freeze-drying methods.[70,71] Aerogels have several distinctive characteristics: porosity in the nano-, meso- and macro-scale range with pore volumes of 2–3 cm^3 g^{-1},[72,73] surface areas about 500–600 m^2 g^{-1},[72,73] light weight /low densities of 0.012–0.096 g cm^{-3},[72,73] electrical conductivities of 0.5–0.25 S m^{-1}[70] to 100 S m^{-1},[73] which are various orders of magnitude lower than films of pristine graphene (4,000-15,000 S m^{-1}),[43,74] and Young's moduli of 1.2–6.2 MPa.[72] There is the possibility to: (i) simultaneously dope the aerogel[71,75,76] while reducing the GO and (ii) incorporate metal or metal oxide particles within the aerogel.[26] Nitrogen-boron doped aerogel has been prepared following this methodology with NH_3BF_3 as the reducing and doping agent.[75] **Figure 8**a shows the GO nanosheets used as building blocks of the 3D aerogel shown in Figure 8b. As shown in Figure 8c, the aerogel was highly porous having pores of 3.2-8.5 nm between rGO nanosheets, and pores of 8.5-50 nm between interconnected rGO nanosheets. The capacitance of the nitrogen-boron doped aerogel tested in half-cells in a 1 M H_2SO_4 aqueous electrolyte was 239 F g^{-1} (Figure 8d) - larger than the capacitance of the undoped aerogel (181 F g^{-1}) and graphene paper (142 F g^{-1}).[75] The capacitance, energy density and power density of an all-solid state supercapacitor assembled using PVA/H_2SO_4 electrolyte (Figure 8e) were 62 F g^{-1}, 8.7 Wh kg^{-1} and 1.65 kW kg^{-1}, respectively.[75]

An important concern with the use of aerogels is the final density of electrodes. Pores in ultralight materials are filled with electrolyte, leading to a low volumetric capacitance, as described in.[77] Therefore, densification of aerogels after syn-

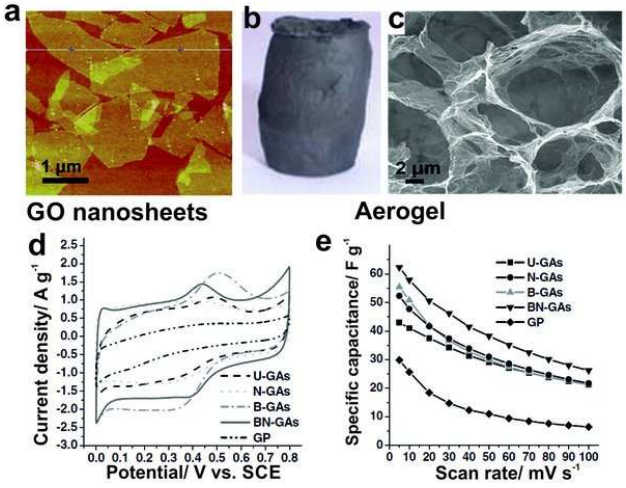

Figure 8. Nitrogen and boron doped rGO aerogel and its capacitive performance.[75] a) Atomic force microscopy images of GO nanosheets used to manufacture the aerogel, (b) optical image and (c) SEM image of the nitrogen-boron doped aerogel, (d) cyclic voltammograms of binder-free electrodes tested at 5 mV s^{-1} in 1 M H_2SO_4 in a half-cell configuration, and (e) capacitance vs scan rate of a full symmetric and all solid state supercapacitor tested using a PVA/H_2SO_4 electrolyte of nitrogen-boron doped aerogel (BN-GAs), and for comparison, un-doped aerogel (U-GAs), nitrogen doped aerogel (N-GAs), boron doped aerogel (BN-GAs), and graphene paper (GP). Reproduced with permission.[75] Copyright 2012, Wiley-VCH.

thesis, filling with redox active particles and infiltration with electrolytes is required for achieving a good volumetric capacitance.

2.1.5. Quantum Capacitance of Graphene

A relatively recent research highlight has been understanding of the quantum capacitance, C_Q, of graphene and its implications on energy storage. The quantum capacitance of graphene has been determined theoretically[78] and experimentally.[79–81] One of the proposed theoretical models to describe quantum capacitance is the two-dimensional free-electron gas model that describes the quantum capacitance as a function of carrier concentration, Fermi velocity, temperature, potential of graphene (V), and other fundamental physical quantities.[82] This model predicts a C_Q vs V curve with the following characteristic: (i) it has a minimum at the Dirac point or point of zero charge where $C_Q = 0.8$ μF cm^{-2}, (ii) C_Q increases linearly with V, and (iii) it is symmetric respective to the Dirac point.[82] However, as shown in **Figure 9**a, the experimentally determined C_Q vs V curve of graphene shows a round rather than V-shaped minimum, which is larger than predicted by the model.[82] This difference has been associated with the presence of impurities on graphene that cause local potential fluctuations or electron/hole puddles.[82,83] Figure 9a shows a fitting of the experimentally measured quantum capacitance with a free-electron gas model that considers a carrier concentration

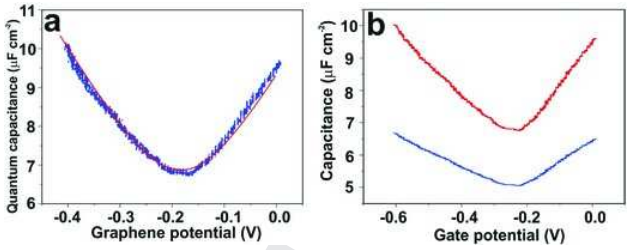

Figure 9. Quantum capacitance of graphene measured in BMIM PF_6.[82] (a) Measured quantum capacitance (blue dots) and fitting of a free-electron gas model (red line), (b) capacitance of graphene as a function of gate potential where the total capacitance is the blue line and the quantum capacitance is the red line. The double layer capacitance (not shown) is 21 μF cm^{-2}. Reproduced with permission.[82] Copyright 2009.

term induced by impurities. The measured capacitance C at a graphene-electrolyte interface (also called interfacial capacitance) has been modeled as

$$C = \frac{1}{C_Q} + \frac{1}{C_D}, \quad (4)$$

where C_Q is quantum capacitance and C_D is a double layer capacitance. According to this model, the smaller term C_Q or C_D dominates the total capacitance C. C_D is generally larger than C_Q and remains constant with gate potential. Therefore, as shown in Figure 9b, C_Q dominates the overall capacitance C and $C < C_Q < C_D = 21$ μF cm^{-2}. Hence, according to this model and the fact that $C_Q < C_D$: (i) the presence of quantum capacitance brings down the overall interfacial capacitance of graphene-based materials, and (ii) the variation of C is directly proportional to the variation C_Q.

Studies show that quantum capacitance may be a main component of the overall measured interfacial capacitance at carbon-aqueous electrolyte interfaces. First, it has been pointed that the shape of the measured capacitance vs potential curve of a pyrolytic graphite-NaF/water interface resembles that of graphene-NaF/water interface which has been modeled considering a quantum capacitance contribution.[82] In the past, this interfacial capacitance was explained in terms of a space-charge capacitance model applied to semiconductors.[46] However, this model failed to explain the shape of the interfacial capacitance vs potential curve.[46] Second, it is known that carbons with an increased specific surface area due to microporosity (<2 nm) do not show a proportional increase in capacitance. Traditional understanding attributes this phenomenon to inaccessible surface area of micropores to the electrolyte. This behavior of carbons has been observed on high specific surface area and microporous a-MEGO that had a lower areal capacitance than rGO with a lower specific surface area and no micropores.[80] It has been suggested that this may be correlated to the presence of single or few-layers thick micropore walls, i.e., graphene-like structures that may have a contribution to quantum capacitance. As previously explained, a quantum capacitance component (Equation (4)) smaller than the double

layer capacitance component can bring down the overall interfacial capacitance C.[80]

The variation of the overall capacitance C of graphene (Equation (4) using a Helmholtz capacitance C_H instead of C_D) with the number of layers was studied.[81] C_Q was theoretically determined and shown to increase with the number of graphene layers, saturating at 5 layers. The former was attributed to an increased density of states as more graphene layers are stacked, and the latter was attributed to a screening effect causing charge accumulation at the outer-most layers. From numerical calculations using an experimentally applied potential and measured C, C_H was found to decrease with increasing number of graphene layers. These trends of C_Q and C_H resulted in a larger overall interfacial capacitance C for SL-graphene as compared to FL-graphene.

Further evidence of quantum capacitance playing a role in energy storage process undergone by graphene and rGO is the effect of overall capacitance increase with nitrogen-doping. This has been generally attributed to the pseudocapacitance activity of the incorporated nitrogen atoms. However, recent studies suggest that quantum capacitance plays a role in all kinds of carbons incorporating thin graphene-like walls, such as carbide-derived carbons.[84] Nitrogen doping increases the quantum capacitance of CVD grown graphene as compared to pristine graphene from 2.5 μF cm^{-2} to ≈ 4.6 μF cm^{-2}.[80] This has been attributed to the increase of carrier density in the graphene lattice due to the surplus of electrons supplied by the doping nitrogen atoms.[80] In accordance with Equation (4), it was inferred that the increase of interfacial capacitance C of nitrogen-doped a-MEGO, from 6.0 μF cm^{-2} (non-doped) to 22.0 μF cm^{-2} (2.3 atom % doped) may be correlated with the increase of quantum capacitance, C_Q, at nitrogen-doped graphene-like micropore walls.[80] In summary, heptagonal and pentagonal defects, vacancies, ad-atoms and functional groups lead to an increase of quantum capacitance, to the expense of decreasing the electrical conductivity of graphene.

The investigations of quantum capacitance have: (i) unveiled answers to long-standing questions, (ii) posed new challenges both for theoretical and experimental scientists, and (iii) put forward new ideas about the design of graphene-based devices. Capacitance is also highly influenced by the size of the 2D channels (slit pores) as outlined in the next section.

2.1.6. Capacitance in 2D Nanochannels

The sharp increase of capacitance in pores of subnanometer size was first studied using carbide-derived carbons in organic electrolytes.[60,85] It was found that the maximum capacitance was reached when the pore size approached the desolvated ion size,[86] i.e., contrary to a long-held traditional view, desolvated ions entered subnanometer pores. This major breakthrough stimulated the development of new theoretical models (see equations in **Figure 10**b) to explain capacitance in nanoporous carbons[87] and further experimental studies that confirm that this phenomenon occurs in other forms of carbon and other type of electrolytes that involve electrolyte nanoconfinement. Graphene is not the exception, and molecular dynamics simulations have shown a sharp increase of capacitance in sub-

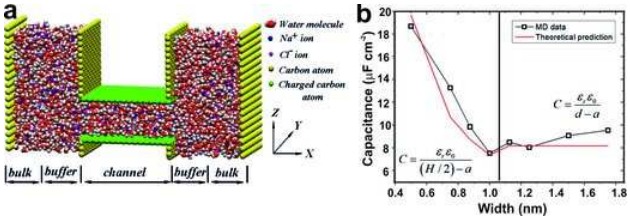

Figure 10. a) Schematic of a molecular dynamics model of a graphene nanochannel filled out with a 4 M NaCl solution.[88] The dimensions of the system in x, y, and z directions are 10.1, 2.84, and 5.0 nm, respectively. The channel length is 3.81 nm. Bulk and buffer regions are considered in the model for equilibration, (b) capacitance vs pore width calculated from molecular dynamics simulations and theoretical calculation according to displayed equations (variables described in[88]). a–b) Reprinted with permission from (Journal of Physical Chemistry C **2015**, 119, 23813). Copyright 2015, American Chemical Society. Q9

nanometer 2D channels of graphene in a NaCl/H_2O electrolyte (Figure 10).[88] These findings point towards the design of 2D nanochannels that are ion-selective as a means to optimize capacitance..

2.1.7. Concluding Remarks

In summary, research has demonstrated that it is the modification of lattice structure, texture, morphology and chemistry of pristine graphene that leads to enhanced energy storage. Perfect planar graphene sheets offer a low capacitance. Open porosity and curved morphology of graphene nanosheets were found to favor suitable ion transport leading to both high energy and power densities. Electrolyte access was favored by electrodes with an in-plane geometry. Graphene-based materials provide primarily double layer capacitance and pseudocapacitance was introduced by doping and chemical functionalization intrinsic to rGO synthesis. Defects and dopants increase quantum capacitance of graphene. However, even higher capacitances can be achieved with other 2D nanomaterials that are primarily pseudocapacitive, as described next.

2.2. 2D Metal Oxides

Metal oxides are attractive for capacitive energy storage due to their redox activity that raises their capacitance values above those for classical EDLCs. Their larger specific weight compared to carbon offers high volumetric capacitance, even when the gravimetric capacitance is in the same range as for carbon. A main drawback is that most of metal oxides used are insulators or semiconductors, offering a lower electrical conductivity as compared to carbons. This limits their energy storage capability, especially at high rates. Defects and non-stoichiometry often increase the electronic conductivity. Proper design of nanosheet morphology and texture (Figure 1), and electrode architecture **(**Figure 4**)** can facilitate ion transport whereas electrical conductivity can be improved by hybridization of metal oxide nanosheets with other electrically conductive nanostruc-

tures (Figure 2). Moreover, capacitive properties are brought up by the two-dimensionality in metal oxides that in the bulk state are better suitable for battery applications. In addition, 2D metal oxides can be used as building blocks for 3D electrode architectures that enable enhanced energy storage performance.

2.2.1. 2D Ruthenium Oxide

Hydrous ruthenium oxide has very high capacitance due to a combination of electrochemical double layer capacitance and redox pseudocapacitance related to a dual electron and proton exchange in acidic electrolytes. It also has a higher electronic conductivity as compared to most other oxides.[89] Ruthenium oxide nanosheets have been obtained by the exfoliation of ruthenic acid $H_{0.22}RuO_{2.11}\cdot nH_2O$, obtained by acid treatment of potassium or sodium ruthenates, using ion intercalation of bulky ions such as tetrabutylammonium in aqueous solutions.[90–92] As shown in **Figure 11**a, the ruthenic acid precursor has a ruthenic acid backbone, which was crystalline and electrically conducting, with a hydrated interlayer that allows proton conductivity.[90–92] As studied by cyclic voltammetry, this structure enabled an overall capacitance of 392 F g^{-1} at 2 mV s^{-1} in 0.5 M H_2SO_4 with contributions from double layer capacitance of 200 F g^{-1} (shaded region in CV in Figure 11c) and redox activity (peaks in CV in Figure 11c).[90] Ruthenic acid nanosheets (Figure 11b) showed a capacitance of 658 F g^{-1} at 2 mV s^{-1}, which is similar to that of hydrous RuO_2 and ten times larger than that of nanocrystalline anhydrous RuO_2.[90,92] Similar to the ruthenic acid precursor, ruthenic acid nanosheets showed a contribution from double layer capacitance of 200 F g^{-1} (shaded region in Figure 11d), but an enhanced redox activity (larger peaks in Figure 11d).[90] The latter was attributed to a more open architecture of nanosheets that enabled improved ion transport resulting in an increased net redox pseudocapacitive activity.[90,93] Cycling stability was demonstrated up to 10,000 cycles.[90–92,94] Flexible and transparent films of ruthenic acid nanosheets were manufactured by electrophoretic deposition.[94]

Solution-based composites of rGO and ruthenic acid nanosheets have been prepared in order to prevent the restacking of the ruthenic acid nanosheets and improve electrochemical utilization.[95] The capacitance increased from 633 F g^{-1} for ruthenic acid nanosheets alone to 998 F g^{-1} for the ruthenic acid nanosheets in the rGO (60 %) -ruthenic acid nanosheets (40 %) composite in 0.5 M H_2SO_4.[95] While RuO_2 achieves high capacitance, the cost and need for using acidic electrolytes limit its application. However, RuO_2 nanosheets are also electrochemically active in AcOH-AcOLi buffered solutions and biocompatible electrolytes, such as fetal bovine serum.[93]

2.2.2. 2D Manganese Oxide

MnO_2, unlike RuO_2, is a common and inexpensive material, showing a similar pseudocapacitive behavior. Manganese oxide nanosheets have been synthesized using several methods. Early studies used the top-down approach cited above that involved intercalation of first H^+ and then bulky ions such as tetramethylammonium (TMA) into layered precursors

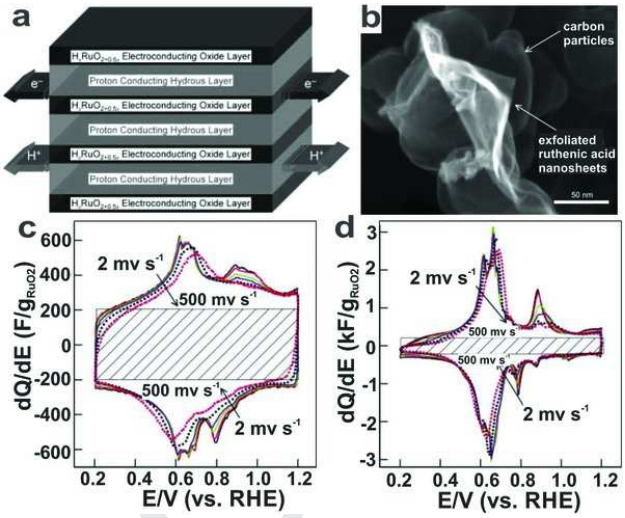

Figure 11. 2D ruthenic acid nanosheets and their supercapacitor performance.[90] a) schematic describing the concept of the mixed proton-electron conductivity of layered ruthenic acid hydrate, (b) SEM image of ruthenic acid nanosheet supported on carbon particles, (c, d) cyclic voltammograms of layered ruthenic acid hydrate (c) and ruthenic acid nanosheets (d) in a 0.5 M H_2SO_4 electrolyte at sweep rates from 2 to 500 mV s^{-1}. The contribution of double-layer capacitance is indicated by shaded regions in (c, d). Reproduced with permission.[90] Copyright 2003, Wiley-VCH Verlag.

such as $K_{0.45}MnO_2$ resulting in swelling and delamination.[96,97] Other methods use a bottom-up chemical synthesis approach where Mn^{2+} ions are oxidized in the presence of TMA[98,99] or MnO_4^- ions are reduced in the presence of organic reducing agents.[100,101] The main disadvantages of these methods are the multi-step and time-consuming procedures and the difficulty to remove 100 % of the intercalant ions/molecules. Both methods produce colloidal solutions of nanosheets of submicrometer to micrometer width and thicknesses in the subnanometer range implying few-layers nanosheets incorporating water.[98–100] However, a tendency to re-stack after carrier-liquid removal persists and most of these studies showed aggregates of nanosheets rather than individual nanosheets.[97–99] Their morphology can sometimes resemble a flower.[98,101] Recently, MnO_2 nanosheets were synthesized by a single-step liquid-phase exfoliation method that produces a mix of flat and flower-like nanosheets.[102] Challenges in the synthesis of MnO_2 nanosheets include the control of thickness distribution, lateral size, removal of non-delaminated particles and elimination of re-stacking of the sheets upon removal of the carrier liquid.[97–99]

The capacitive performance of MnO_2 nanosheets is determined by their morphology, degree of crystallinity and adequate electrolyte access to the surface. A curved or flower-like morphology favors electrolyte access. It is known that the presence of physisorbed water in amorphous MnO_2 favors proton and ion transport.[103] Most MnO_2 nanosheets produced to date were amorphous or had poor crystallinity.[27,101] Capacitances

up to 532.5 F g^{-1} have been reported for electrodes of solely MnO_2 amorphous nanosheets (5–20 nm width) tested in 1 M Na_2SO_4 and in a half-cell configuration.[100] This capacitance was larger than that for MnO_2 spheres and nanorods.[100]

Due to the semiconducting nature of MnO_2 and tendency of nanosheets to re-stack, hybridization with other electrically conducting nanosheets or other nanomaterials is suggested (Figure 2**)**. A hybrid of amorphous MnO_2 nanosheets and graphene produced by liquid-phase co-exfoliation had capacitances of 300 F cm^{-3} (217 F g^{-1}) in a 0.5 M K_2SO_4 electrolyte.[27] Another rGO-MnO_2 nanosheet hybrid achieved a capacitance of 188 F g^{-1} in 1 M Na_2SO_4.[104] An improved performance has been achieved by an MnO_2-rGO nanosheet hybrid with an interdigitated microsupercapacitor configuration described in Section 3.3.[28]

High capacitances and power performance have been reported for a hierarchical assembly of 3D nanostructures of MnO_2 nanosheets vertically grown on an Au layer deposited onto Co_3O_4 vertically aligned nanowalls,[105] and vertically aligned MnO_2 nanosheets onto carbon-coated Co_3O_4 nanorods.[106] However, as described in Section 2.2.4., Co_3O_4 is a material that has contributions from battery-type energy storage mechanisms and, therefore, cannot be considered truly pseudocapacitive. In addition, the synthesis methods utilized in these works involve multi-step procedures such as electrodeposition and sputtering that may neither be cost-effective nor allow for scalability. Printing is a more scalable manufacturing approach and is relevant for the manufacture of flexible supercapacitors. A flexible printed asymmetric supercapacitor made of rGO as anode, MnO_2 nanosheets as cathode, and $Ca(NO_3)_2$-SiO_2 composite gel electrolyte showed a capacitance of 175 F g^{-1} at 0.1 A g^{-1} and maximum energy density of 97.2 Wh Kg^{-1}.[101]

In summary, MnO_2 should be combined with graphene or other conducting materials for achieving high capacitance values. With a proper design of material architecture, it can be used in both, small scale and large-scale devices. Its low cost, compared to other transition metal oxides, makes it an attractive candidate for large-scale energy storage applications.

2.2.3. 2D Molybdenum Oxide

Among other transition metals showing pseudocapacitive behavior, molybdenum trioxide is attracting much attention due to potentially high volumetric capacitance. MoO_3 is a material that can store charge by various mechanisms including double layer capacitance, redox pseudocapacitance, ion intercalation pseudocapacitance and diffusion controlled ion intercalation.[107,108] Multi-layered 2D α-MoO_3 of typical dimensions of 100 nm x 40 nm x 21 nm was synthesized by liquid-phase exfoliation, mixed with SWCNTs, and its charge storage properties were investigated in $LiClO_4$/PC electrolyte in a 1.5–3.5 V electrochemical window.[109] This composite stored up to 375 C g^{-1} charge at 20 mV s^{-1}, similar to that of mesoporous α-MoO_3[107] and α-MoO_3 nanobelts,[108] but with a larger contribution from diffusion controlled Li-ion intercalation.[110] This was attributed to a larger number of intercalation sites available due to the 2D nature, as compared to nanobelts. Hexagonal MoO_3

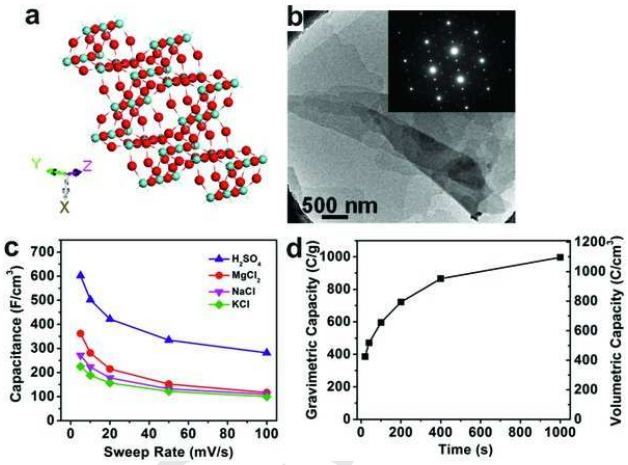

Figure 12. 2D h-MoO_3 and its supercapacitor performance.[111] a) Model of the crystal structure of h-MoO_3 where green dots represent Mo atoms and red dots represent O atoms, (b) TEM image and diffraction pattern of a h-MoO_3 nanosheet, (c) volumetric capacitance vs scan rate curves of h-MoO_3 film electrodes tested in various aqueous electrolytes, (d) gravimetric and volumetric charge vs charging time curve of a h-MoO_3 film electrode tested in a 1 M $LiClO_4$/EC/DMC electrolyte. Reproduced with permission.[111] Copyright 2016, Nature Publishing Group. .

nanosheets (h-MoO_3, **Figure 12**a) were produced using coating of peroxomolybdate onto NaCl that served as template to guide the growth of the oxide upon heat treatment.[111] The area of the nanosheets (Figure 12b) was ≈400 μm^2 and the thickness was tuned from 1.6 nm to 16 nm by controlling the precursor/salt ratio. As shown in Figure 12c, film electrodes (without electrically conducting additive) of h-MoO_3 nanosheets tested in a half-cell configuration showed a high volumetric capacitance up to 600 F cm^{-3} in various aqueous electrolytes. As shown in Figure 12d, when tested in a 1 M $LiClO_4$/EC/DMC electrolyte, the h-MoO_3 nanosheets electrodes stored a total of 996 C g^{-1} and 1100 C cm^{-3} at 2 mV s^{-1}. This high charge storage was mainly of pseudocapacitive nature. A fast high power performance (≈400 C g^{-1} at 100 mV s^{-1}) was attributed to the 2D nature that facilitated a fast ion transport. It was demonstrated that the charge storage scales down with increasing nanosheet thickness, which emphasizes the role of two-dimensionality. A key advantage of this templating method is that 2D nanomaterials with a non-layered crystal structure can be synthesized, which is a requirement for exfoliation methods.

2.2.4. Other 2D Metal Oxides

There are many other oxides than can be produced in a 2D state, including Co_3O_4,[112] $NiCo_2O_4$,[113] TiO_2-B,[114] TiO_2 anatase[115] and Fe_3O_4.[116] However, not all of them can be considered capacitive and caution in this sense should be taken as some of those materials show plateaus in charge–discharge curves that describe battery-type behavior.[117–119]

Metal oxides such as RuO_2, MnO_2 and Nb_2O_5 present true pseudocapacitive behavior (also named intrinsic pseu-

docapacitance) typical of that observed for a capacitive carbon electrode.[118] Mn_3O_4, Fe_3O_4 and $MnFe_2O_4$ are true pseudocapacitors with a modest capacitance.[118] TiO_2(B) and T-Nb_2O_5 present intrinsic intercalation pseudocapacitance.[118] Some metal oxides that in bulk state behave like battery materials, such as $LiCoO_2$, V_2O_5 and TiO_2 (anatase phase), present "extrinsic" pseudocapacitive behavior when nanostructured (plateaus in charge–discharge curves are completely replaced by almost linear regions).[118]

V_2O_5 is attractive for energy storage applications due to its multiple valence states and layered structure. Although typically considered for battery applications while in its bulk state, nanostructuring brings out its pseudocapacitive properties described by sloping discharge curves and broad and featureless CVs.[118] V_2O_5 nanosheets of lateral dimensions up to 10 μm and thickness of 4 nm have been synthesized using hydrothermal methods and the nanosheets were then utilized to build a 3D structure using freeze-drying.[120] Symmetric devices of the 3D V_2O_5 showed a capacitance of 451 F g^{-1} at 0.5 A g^{-1} in a 1 M Na_2SO_4 electrolyte in a 2 V electrochemical window.[120] A similar performance has been achieved for hybrids of V_2O_5 nanosheets and reduced graphene oxide.[121]

Other metal oxides such as Co_3O_4, $NiCo_2O_4$ and $MnCo_2O_4$ undergo both battery-type and pseudocapacitive process in aqueous electrolytes (a discharge curve with plateaus and sloping regions).[118] A fast response with an enhanced pseudocapacitive contribution can be obtained when nanostructured.[118] This is the case of $Ni(OH)_2$ and $Co(OH)_2$, which in the bulk state have a battery-type behavior and, in fact, are materials commonly used in alkaline batteries. When nanostructured, they show a combination of plateaus (battery-type behavior) and sloping regions (pseudocapacitive behavior) in charge–discharge curves. This has led to confusion in the literature where often they have been incorrectly referred to as "pseudocapacitors" or "supercapacitors".[118] Since these materials still undergo phase transformations they cannot be truly pseudocapacitive[119] and thus they are not included in this review. Moreover, they are often used in hybrid devices as the battery electrode that is combined with a capacitive electrode, such as carbon.[119]

2.3. 2D Transition Metal Dichalcogenides

Transition metal dichalcogenides are a large family of 2D materials that include many semiconducting and even metallic structures showing promise for energy storage applications.[6] MoS_2 is the most common transition metal dichalcogenide, also called molybdenite, which has 2H (semi-conducting), 1T (metallic), both metastable, and 3R (stable at standard conditions) polytypes.[122] 2D MoS_2 has been produced using a variety of synthesis techniques including chemical and electrochemical exfoliation.[6,123,124] These processes rely on the intercalation of Li-ions into the bulk MoS_2 followed by exfoliation in water.[123,125] Chhowalla et al. showed that chemical exfoliation yields 100 % monolayer MoS_2, of which, ≈70 % is transformed from 2H to 1T phase upon Li-ion intercalation.[123] **Figure 13**a shows a STEM image of a 1T-MoS_2 nanosheet where the 1T crystal arrangement can be appreciated and Figure 13b shows a SEM image of a film electrode made of 1T-MoS_2 nanosheets. 1T-MoS_2 showed capacitive behavior in aqueous H_2SO_4, Li_2SO_4, Na_2SO_4 and K_2SO_4 (Figure 13c) and organic electrolytes.[18] Binder-free 1T-MoS_2 electrodes tested in half-cells showed volumetric capacitances up to 650 F cm^{-3} (Figure 13d) at scan rate of 20 mV s^{-1} with a capacity retention of 97 % over 5,000 cycles.[18] This was attributed to ion intercalation into the 1T-MoS_2 layers due to their hydrophilicity and metallic character. 1T-MoS_2 also intercalated larger ions as it was shown for symmetric devices with capacitances of 199 F cm^{-3} in TEA BF_4/MeCN and 250 F cm^{-3} in EMIM BF_4/MeCN with capacity retention of 90 % over 5000 cycles.[18] The maximum energy and power density of this device were 0.11 Wh cm^{-3} and 51 W cm^{-3}, respectively.[18] Microsupercapacitors of 2D MoS_2 nanosheets and VS_2 nanosheets are described in Section 3.2.2.

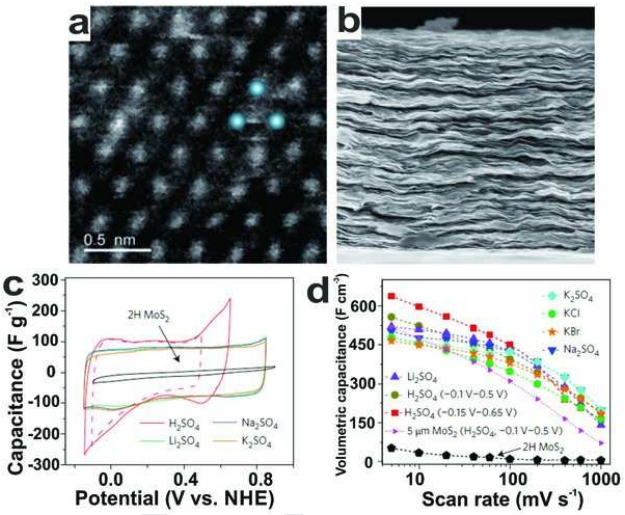

Figure 13. 2D 1T-MoS_2 and its supercapacitor performance.[18] a) Dark field STEM image of a 1T-MoS_2 nanosheet where blue spheres indicate Mo atoms, (b) SEM image of an electrode made of 1T-MoS_2 nanosheets by vacuum filtration, (c) cyclic voltammograms of 1T-MoS_2 nanosheet electrodes showing capacitive behavior in aqueous electrolytes, and (d) volumetric capacitance vs scan rate for MoS_2 nanosheet electrodes in various aqueous electrolytes. a) Reproduced with permission.[6] Copyright 2013, Nature Publishing Group. b–d) Reproduced with permission.[18] Copyright 2015, Nature Publishing Group.

2.4. 2D Carbides (MXenes)

MXenes are a new family of 2D carbides with metallic conductivity, hydrophilicity, and capability for ion intercalation that have shown high volumetric capacitances in microsized, binder-free, and mechanically strong electrodes.[17,126] MXenes are derived from MAX phases with the $M_{n+1}AX_n$ composition, where M is an early transition metal (Mo, Ti, Nb), A is an element from groups IIIA or IVA (Al, Ga, Si, Ge, Sn), X is C or N, and n = 1, 2, 3. More than 70 MAX phases[7,127] and about the same number of solid solutions and multi-element layered

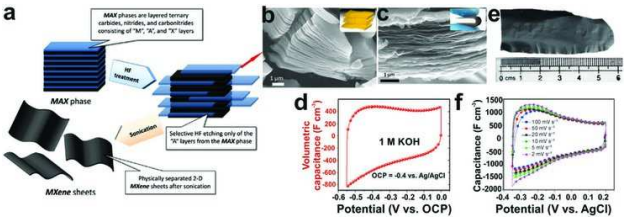

Figure 14. MXenes and their electrochemical properties. a) Schematics showing the manufacturing process, (b) SEM image shows a multilayer $Ti_3C_2T_x$ obtained after etching Al from Ti_3AlC_2 using HF,[11] (c) SEM image of $Ti_3C_2T_x$ paper obtained by vacuum assisted filtration of $Ti_3C_2T_x$ sheets; the inset shows its flexibility,[11] (d) cyclic voltammogram of $Ti_3C_2T_x$ paper in 1 M KOH,[11] (e) $Ti_3C_2T_x$ film manufactured by rolling clay-like $Ti_3C_2T_x$ obtained by etching Al out of Ti_3AlC_2 with a mix of LiF and HCl,[126] (f) cyclic voltammograms showing high volumetric capacitance of clay-like $Ti_3C_2T_x$ in 1 M H_2SO_4.[126] a) Adapted with permission.[7] Copyright 2015, American Chemical Society. b–d) Reproduced with permission.[11] Copyright 2013, AAAS. e, f) Reproduced with permission.[126] Copyright 2014, Nature Publishing Group..

structures[8,128] have been produced, providing a large number of potential precursors for MXene synthesis. As shown in **Figure 14**a, $M_{n+1}X_n$ or MXenes are obtained by etching away the A element from the MAX phase. This was achieved for the first time by treating Ti_3AlC_2 with hydrofluoric acid (HF) to produce a multilayer $Ti_3C_2T_x$ (Figure 14b) followed by sonication that produces delaminated MXene sheets (Figure 14c).[9] This treatment induces the presence of chemical functionalities T_x on the delaminated MXene surfaces including = O, –OH, and –F groups.[9,129] These surface functionalities influence the electronic properties of MXenes and induce hydrophilicity.[7,10] Importantly, MXenes can intercalate ions and organic molecules;[11,130] this property was used to delaminate multilayer MXenes into single- or few-layer sheets by intercalation of dimethyl sulfoxide (DMSO)[130] or tertiary amines[131,132] followed by sonication in water.

Most research on MXenes to date has been focused on $Ti_3C_2T_x$ even though about 20 different MXenes have already been produced. $Ti_3C_2T_x$ films have a metallic conductivity of 2.4×10^5 S m^{-1}[17] and show spontaneous intercalation upon immersion into solutions, and capacitive behavior in a variety of aqueous electrolytes including sulfates, hydroxides and nitrates of Na^+, K^+, Li^+, Al^{3+}, Mg^{2+}, with capacitances up to 350 F cm^{-3} for binder-free $Ti_3C_2T_x$ paper (Figure 14c) tested in 1 M KOH electrolyte (Figure 14d).[11] A significant advance in the science of MXenes is the use of alternative methods, other than HF, to selectively etch away aluminum from the MAX phase. Recently, Ti_3C_2 was produced by using a solution of LiF + HCl as an etchant.[126] This methodology favored the intercalation of water and Li ions, which in turn, conferred the material a clay-like texture that allowed its rolling into free-standing films (Figure 14e). When tested in 1 M H_2SO_4, these films showed a high volumetric capacitance of up to 900 F cm^{-3} (Figure 14f), and high gravimetric capacitance of 246 F g^{-1}. Cycling stability was demonstrated for 10,000 cycles at 10 A g^{-1}. The improved performance of these films in respect to the HF-etched Ti_3C_2 was attributed to water molecules and Li ions incorporated between the MXene layers and improving ion access to MXene surfaces.

MXenes not only provide a high storage capacity but also deliver it at high rates. Unlike storage processes in battery materials that are limited by Li-ion diffusion, MXenes store charge by cation adsorption into swollen MXene galleries, due to water and electrolyte ions intercalated in between MXene layers, accompanied and facilitated by rapid layer expansion and contraction.[13] Pseudocapacitive storage mechanisms include a reversible change in the oxidation state of the M element, as it has been demonstrated for $Ti_3C_2T_x$ in 1 M H_2SO_4.[133] This redox process lead to the very high volumetric capacitance of 900 F cm^{-3}, at a low (<100 m^2 g^{-1}) specific surface area determined by nitrogen gas adsorption.[126] Moreover, high volumetric capacitances are maintained for thick electrodes (≈550 F cm^{-3} and ≈380 F cm^{-3} for electrodes with thicknesses of 30 μm and 75 μm, respectively).[126] This implies that MXenes are suitable for manufacturing both, microsized and conventional supercapacitors. The presence of chemical functionalities on MXenes can be exploited to further enhance energy storage. It has been found that removal of fluorine functionalities and substitution for oxygen containing functionalities increased gravimetric and volumetric capacitance (in 1 M H_2SO_4) of $Ti_3C_2T_x$ immersed in KOH or KAc.[134]

Delaminated MXenes have been processed into free-standing films that, due to the combination of suitable electrical conductivity, hydrophilicity, tensile strength and flexibility, show promise for flexible supercapacitor applications. A $Ti_3C_2T_x$/PVA-KOH composite film achieved a volumetric capacitance of 530 F cm^{-3} at 2 mV s^{-1} (much higher than ≈100 F cm^{-3} for graphene[23]), electrical conductivity of 2.2×10^4 S m^{-1}, tensile strength of 30 MPa and Young's modulus of 3 GPa.[17] A strategy to overcome the natural tendency of delaminated MXenes to re-aggregate has been the introduction of separating particles that include onion-like carbon (0D), carbon nanotubes (1D) and graphene (2D) in sandwich-like assembled films.[30] $Ti_3C_2T_x$/onion-like carbon (397 F cm^{-3}), $Ti_3C_2T_x$/SWCNTs (390 F cm^{-3}), and $Ti_3C_2T_x$/graphene (435 F cm^{-3}) sandwich-like films showed improved volumetric capacitance as compared to the pure $Ti_3C_2T_x$ (360 F cm^{-3}) in 1 M $MgSO_4$.[30] In situ polymerization of pyrrole between MXene sheets increased capacitance beyond 1000 F cm^{-3} due a synergy between two pseudocapacitive materials proving energy storage in both, $Ti_3C_2T_x$ and polypyrrole.[32] Binder free MXenes can be used as current collector-free electrodes due to their high metallic conductivity, minimizing the amount of inactive materials and further increasing the energy density of the device. However, the key issue for MXenes use as pseudocapacitive material is finding a matching positive electrode with equally high capacitance and conductivity, as they can only operate under negative potentials in aqueous electrolytes.

Li-ion and Na-ion capacitors using MXenes (Ti_2C, V_2C and other) with organic electrolytes allow expanding the voltage window and are a promising research direction.[131,135] It has also been shown that $Ti_3C_2T_x$ can work with common organic

electrolytes.[136] Also, more than a dozen of MXenes already available now should be evaluated, as thinner M_2C structures should offer a higher gravimetric capacitance, while Mo, Nb and V containing MXenes may experience a larger change in the oxidation state, compared to Ti, and provide a higher redox capacitance.

2.5. Materials Summary and Applications

Table 1 summarizes the performance of the various 2D nanomaterials reviewed here. Among the graphene-based materials, a-MEGO had the largest gravimetric energy and power densities that reach far beyond the performance of commercial activated-carbon supercapacitors that have an energy density of ≈5 Wh kg^{-1} and power density of 800–1200 W kg^{-1}[137] and, thus, is suitable for large scale energy storage applications. Moreover, a-MEGO in combination with mixed ionic liquids can be used for devices operating under extreme weather conditions (−50°C to 80°C). PECVD-grown graphene is suitable for AC-line filtering application, where operation at high frequencies is necessary. Aerogels based on rGO are promising for the development of all-solid-state supercapacitors, and their doping can add pseudocapacitance. As described in the next section, adequate electrode design makes rGO suitable for microsupercapacitor applications, where the volumetric and areal capacitances are critical.

2D transition metal oxides and transition metal dichalcogenides offer larger gravimetric capacitances than graphene-based 2D nanomaterials and can be suitable for both large- and small-scale applications. Ruthenic acid nanosheets have the highest capacitance and a high gravimetric and volumetric energy and power densities, which make them suitable for microdevice applications. The electrical conductivity and transparency of these nanosheets make them also suitable for use in energy storing windows and screens. Manganese oxide nanosheets are suitable for both large scale and thin-film based supercapacitors, when hybridized with an electrically conducting component. MoO_3 nanosheets with high volumetric capacitance are suitable for thin-film devices. Moreover, MoO_3 nanosheets are active in a variety of aqueous and organic electrolytes. The same can be said about transition metal dichalcogenides, as demonstrated for 1T-MoS_2, which is suitable for manufacturing binder-free electrodes due to their metallic conductivity. 2D carbides, such as $Ti_3C_2T_x$, combine highly desirable characteristics for supercapacitors including metallic conductivity, flexibility, mechanical stability and redox-active surfaces, which lead to a high volumetric capacitance delivered at high rates, even for electrodes with thicknesses in the order of tens of micrometers. These materials are especially promising for binder-free flexible devices and microsupercapacitors.

As described in the next section, the realization of all these applications relies not only on materials design, but also strongly depends on the electrode architecture, device configuration and manufacturing approaches.

3. Electrode Architecture, Device Design and Manufacturing

Electrode design and device configuration are crucial for maximizing the performance of supercapacitors based on 2D nanomaterials. In this section, various aspects of design, architecture and manufacturing of 2D nanomaterials-based electrodes and full supercapacitors are discussed.

3.1. Nanosheet Morphology and Device Configuration

Early studies on the application of graphene for supercapacitors showed that the stacking of nanosheets hindered electrolyte access (Figure 1a). This problem was alleviated by: (1) modifying the nanosheet morphology from flat to curved **(Figure 1b)**, which prevented the nanosheets from restacking[138] and (2) introducing mesoporosity using a carbon activation process that generated a network of micro- and mesopores (Figures 1d and 7d),[23] and (3) manufacturing of electrodes with an "in-plane" geometry[45] which is the focus of this section. In a typical "sandwich configuration" (Figure 4a), nanosheets are stacked onto current collectors that face each other. In this configuration the transport of electrolyte ions across nanosheets is difficult. In contrast, when nanosheets are vertically aligned with respect to current collectors (Figure 4b), the electron transport trough inter-sheet spaces is more efficient. The literature describes the latter configuration (Figure 4b) as "in-plane" geometry.[45] This can be interpreted as the ion transport direction respect to the basal plane of the nanosheet, i.e., "in-plane" geometry refers to the transport of ions in a direction parallel to the basal plane of the nanosheet. Conversely, the configuration in Figure 4a, is said to have an "out-of-plane" geometry, i.e., where the ion transport direction is orthogonal to the basal plane of the nanosheet. In an interdigitated configuration (**Figure 4c**), typically used for microsupercapacitors, electrodes of stacked nanosheets lie side by side (usually separated by few-micrometer distances) in the same plane of the current collector (thus described as in-plane electrodes). The electrolyte is deposited on top and in between the electrodes, so that the ion transport occurs along the basal plane of the nanosheets. This geometry favors a faster ion transport as it utilizes the 2D channels between nanosheets, optimizing the utilization of the active surface area. This leads to enhanced energy and power densities.

3.2. Microsupercapacitors, Flexible and Freestanding Film Supercapacitors

Besides their high surface area, one of the main attractive features of 2D nanomaterials is their flexibility allowing bending and folding. The 2D nature of these materials allows manufacturing of flexible and freestanding film devices that keep their charge storage properties unaltered after bending and folding. When combined with solid-state electrolytes, 2D nanomaterials are suitable for manufacturing flexible all-solid state supercapacitors.

The combination of flexibility with high electrical conductivity makes 2D nanomaterials particularly attractive for manufac-

Table 1. Summary of 2D nanomaterials

Material	Electrochemical performance	Electrode thickness	Configuration	Electrolyte
Liquid-phaseexfoliated graphene[43]	543 μF cm^{-2}, 12 F g^{-1}, 2.3 ms cap. resp.	350 nm	half cell	1 M H_2SO_4
PECVD graphene[22]	97.5 μF cm^{-2},3 Fcm^{-3},8.3 ms cap. resp.	600 nm	symmetric device	25 % KOH/H_2O
CRGO[49]	100 F g^{-1}	-	symmetric device	TEA BF_4/MeCN
MEGO[52]	191 F g^{-1}	-	symmetric device	5 M KOH
TEGO[54]	264 F g^{-1}	-	symmetric device	5.5 M KOH
TEGO[54]	122 F g^{-1}	-	symmetric device	[$MeEt_3N$]BF_4/MeCN
a-MEGO[23]	60 F cm^{-3}, 166 F g^{-1}, 70 Wh kg^{-1}, 250 kW kg^{-1}, 10,000 cycles	-	symmetric device	BMIM BF_4/MeCN
a-MEGO[56]	150 F g^{-1} at -50 °C- 80 °C	55 mm	symmetric device	PIP_{13}-FSI+PYR_{14}-FSI
Nitrogen-doped graphene[66]	284 F g^{-1} at 5 mV s^{-1} and 226.5 F g^{-1} at 10 A g^{-1}	-	symmetric device	1.0 M [Bu_4N]BF_4/MeCN
Nitrogen-doped graphene + thermal expansion[67]	270 F g^{-1} at 1 A g^{-1} , 182 F g^{-1} at 10 A g^{-1}, 24 Wh kg^{-1}, 1.5 kW kg^{-1}	-	half cell	1 M H_2SO_4
Nitrogen-boron doped rGO aerogel[75]	239 F g^{-1} at 1 mV s^{-1}, ~150 F g^{-1} at 10 mV s^{-1}	1 mm	half cell	1 M H_2SO_4
Nitrogen-boron doped rGO aerogel[75]	62 F g^{-1} at 5 mV s^{-1}, 8.6 Wh kg^{-1}, 1.65 kW kg^{-1}	1 mm	symmetric device	PVA/H_2SO_4
Undoped rGO aerogel[75]	181 F g^{-1}	1 mm	half cell	1 M H_2SO_4
Laser-scribed rGO with round design[139]	0.51 mF cm^{-2}, 3.1 F cm^{-3},4.3×10^{-4} Wh cm^{-3}, 1.7 W cm^{-3}	-	IMS	H_2O in hydrated GO
Free-standing GO films[140]	3.67 mF cm^{-2}, ~ 0.45 F cm^{-3}, 33 ms cap. resp., 10,000 cycles	-	symmetric device	1 M H_3PO_4, PVA/H_3PO_4
Free-standing GO films[140]	5.02 mF cm^{-2}, 276 F g^{-1}, 1.36 x 10^{-3} Wh cm^{-3}, 0.8 W cm^{-3}	-	symmetric device	EMIM BF_4/MeCN
Laser-scribed rGO onto a DVD[141]	2.32 mF cm^{-2}, 3.5 F cm^{-3} at 16.8 mA cm^{-3} , 19 ms cap resp.	-	IMS (16 electrodes)	PVA/H_2SO_4 gel
Laser-scribed rGO onto a DVD[141]	2.35 F cm^{-3}, 1.5×10^{-3} Wh cm^{-3}, 200 W cm^{-3}	-	IMS (16 electrodes)	Ionic liquid/silica
Functionalized rGO + Nafion[144]	118.5 F g^{-1} at 1 A g^{-1}, 110 F g^{-1} at 30 A g^{-1}, 1000 cycles	-	symmetric device	1 M H_2SO_4/Nafion
rGO/niquel nanocone 3D substrate[145]	6.84 mF cm^{-2} at 0.1 mA cm^{-2}, 1.73 F cm^{-3}, 0.15 mWh cm^{-3}, 20,000 cycles	45 μm	symmetric device	PVA-Na_2SO_4 gel
rGO/MWCNTs[152]	6.1 F cm^{-3}, 3.2 ms, 4×10^{-4} Wh cm^{-3}, 77 W cm^{-3}, 3.4 ms cap. resp.	6 μm	IMS	3 M KCl
Free standing rGO/PANI[31]	581 F g^{-1}, 10,000 cycles	-	half cell	1 M H_2SO_4
Free standing rGO/PANI[31]	5.5×10^{-3} Wh cm^{-3}, 3×10^{-2} W cm^{-3}	-	symmetric device	PVA/H_2SO_4 gel
Ruthenic acid nanosheets[90]	658 F g^{-1} at 2 mV s^{-1}, 10,000 cycles	-	half cell	0.5 M H_2SO_4
Ruthenic acid nanosheets + rGO[95]	998 F g^{-1}, 20.3 Wh kg^{-1}, 600 W kg^{-1}	-	half cell	0.5 M H_2SO_4
RuO_2 nanoparticles/ rGO nanosheets[29]	570 F g^{-1}, 20.1 Wh kg^{-1}, 10 kW kg^{-1}, 1,000 cycles	-	half cell	1.0 M H_2SO_4
MnO_2 nanosheets[100]	532.5 F g^{-1}	-	half-cell	1 M Na_2SO_4
MnO_2 nanosheets + graphene[27]	300 F cm^{-3}, 217 F g^{-1}	-	half-cell	0.5 M K_2SO_4
MnO_2 nanosheets/rGO[101]	175 F g^{-1}, 97.2 Wh kg^{-1}, 4 kW kg^{-1}	-	hybrid device	$Ca(NO_3)_2$-SiO_2 gel
dgelO_2 nanosheets/rGO[28]	250 F g^{-1} at 0.5 A g^{-1}, 17.0 Wh kg^{-1}, 2.5 kW kg^{-1}, 7,000 cyles	40 nm	IMS	PVA/H_3PO_4 gel

Table 1. *Continued.*

Material	Electrochemical performance	Electrode thickness	Configuration	Electrolyte
Hexagonal MnO_2 nanosheets/MWCNT paper[146]	91.7 mF cm^{-2}, 1035 F g^{-1} at 2 mV s^{-1}, 572 F g^{-1}, 48.8 mF cm^{-2} at 25 A g^{-1}	-	half cell	0.5 M Na_2SO_4
Hexagonal MnO_2 nanosheets/MWCNT paper[146]	147 F g^{-1}, 17 Wh kg^{-1} , 38 kW kg^{-1}	-	symmetric device	PVA/LiCl gel
Hexagonal MnO_2 nanosheets/MWCNT paper.[146]	25.3 Wh kg^{-1}, 81.0 kW kg^{-1}	-	coaxial device	PVA/LiCl gel
aVA/L_3 nanosheets (21 nm thick)/SWCNTs[109,110]	375 C g^{-1} (pseudocapacitive), 365 C g^{-1} (diffusion controlled), 200 F g^{-1}	-	half cell	1 M LiClO4/PC
h-MoO_3 nanosheets (1.6 nm thick)[111]	600 F cm^{-3}	-	half cell	1 M H_2SO_4
h-MoO_3 nanosheets (1.6 nm thick)[111]	996 C g^{-1}, 1100 C cm^{-3}, 550 F cm^{-3}, 498 F g^{-1}, 0.3 Wh cm^{-3}, 1 W cm^{-3}, 3,000 cycles	1-4 μm	half cell	1 M LiClO4/EC/DMC
3D gel of V_2O_5 nanosheets (4 nm thick)[120]	451 F g^{-1} at 0.5 A g^{-1} and 150 F g^{-1} at 50 A g^{-1}	-	symmetric device	1 M Na_2SO_4
1T- MoS_2 nanosheets[18]	650 F cm^{-3}, 5,000 cycles	-	half cell	1 M H_2SO_4
1T-MoS_2 nanosheets[18]	199 F cm^{-3}, 5,000 cycles	-	half cell	TEA BF_4/MeCN
1T-MoS_2 nanosheets[18]	250 F cm^{-3}, 0.11 Wh cm^{-3}, 1.1 W cm^{-3}	-	half cell	EMIM BF_4/MeCN
MoS_2 nanosheets[142]	8 mF cm^{-2}, 178 F cm^{-3}	0.45 μm	IMS (10 electrodes)	1 M NaOH
VS_2 nanosheets[143]	4.7 mF cm^{-2}, 317 F cm^{-3}, 1,000 cycles	150 nm	IMS	PVA/BMIM BF_4 gel
$Ti_3C_2T_x$ paper[11]	350 F cm^{-3}, 10,000 cycles	-	half cell	1 M KOH
$Ti_3C_2T_x$ film[17]	530 F cm^{-3}	-	half cell	PVA/KOH
Clay-like $Ti_3C_2T_x$[126]	900 F cm^{-3}, 246 F g^{-1} , 10,000 cycles	5 μm	half cell	1 M H_2SO_4
Clay-like $Ti_3C_2T_x$[126]	550 F cm^{-3}, 380 F cm^{-3}	30 μm, 75 μm	half cell	1 M H_2SO_4

turing high-performance microsupercapacitors. Microsupercapacitors are small devices that can be incorporated into microchips, flexible integrated circuits, flexible displays, windows and screens, wearable and portable electronics, sensors, transmitters, and microelectromechanical systems.[14] Microsupercapacitors are typically designed in an interdigitated configuration (Figure 4c) and thus called interdigitated microsupercapacitors (IMSs). Micrometer-sized electrodes are separated by micrometer distances, where the electrolyte is deposited, which implies shorter ion transport distances and diminished overall device resistance. The use of separators and polymeric binders is excluded. The total footprint area may be in the millimeter or centimeter scale and the thickness is typically less than 10 μm.[14] Flexible and freestanding film supercapacitors can occupy a fairly large area (cm^2) or be micro-sized. In the latter case, they can also be called microsupercapacitors.

3.2.1. Microsupercapacitors Based on Reduced Graphene Oxide

Microsupercapacitors based on 2D nanomaterials have shown advantageous features compared to other thin-film energy storage devices. Ajayan et al. reported the fabrication of microsupercapacitors of various geometries by reducing hydrated GO free-standing films with a laser beam.[139] The laser reduced rGO areas constituted the electrode, whereas the non-reduced and hydrated GO areas served as separators and solid state electrolyte. Except for power density, the in-plane devices showed a better performance (see **Table 1**) than the devices manufactured in a sandwich configuration.[139] The in-plane configuration also favored an increased ionic conductivity (2.8×10^{-3} S cm^{-1}).[139] Importantly, the laser scribing induced film porosity, avoiding nanosheet re-stacking, enhancing ionic conductivity and surface area utilization. The ionic conductivity of the non-reduced GO was attributed to oxygen-containing functionalities, making it hydrophilic, and water and ions presence between the GO layers.

In a similar approach, Kaner et al. produced free-standing rGO electrode films using an infrared laser inside a LightScribe CD/DVD optical drive.[140] A symmetric device (sandwich configuration) tested in 1 M H_3PO_4 showed a volumetric capacitance of ~ 0.45 F cm^{-3} with good stability up to a current density of 4.5 A cm^{-3}, an areal capacitance of 3.67 mF cm^{-2} and a response time of 33 ms.[140] A similar device based on activated carbon showed about the same capacitance, but inferior power performance. An all-solid state device in a sandwich configura-

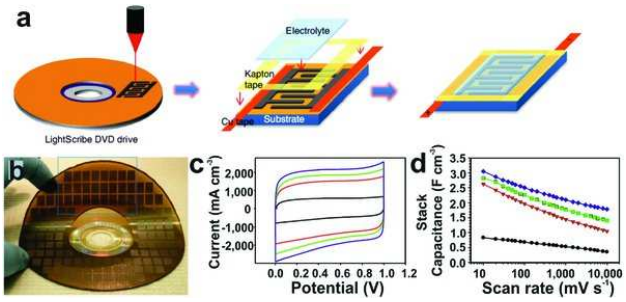

Figure 15. rGO microsupercapacitors manufactured by laser scribing.[141] a) Schematic of the manufacturing process. A GO film is coated onto a PET film that is supported onto a DVD media disc. An interdigitated microsupercapacitor is scribed using a LightScribe DVD burner and electrical contacts and a PVA/H_2SO_4 gel electrolyte area applied, (b) an optical image of a sample of more than 100 microsupercapacitors scribed on a single run, (c) cyclic voltammograms and (d) volumetric capacitance vs scan rate curve of a microsupercapacitor with a sandwich configuration (black line) and interdigitated microsupercapacitors with 4 (red line), 8 (green line) and 16 (blue line) electrodes. Reproduced with permission.[141] Copyright 2012, Nature Publishing Group.

tion incorporating a polyvinyl alcohol (PVA)/H_3PO_4 electrolyte showed similar capacitance and power density with no performance degradation under bending, and 97 % capacitance retention after 10,000 cycles.[140] The use of EMIM BF_4/MeCN as electrolyte enabled a further enhancement of specific capacitance by increasing the voltage window to 4 V.[140] The same group also demonstrated a high throughput fabrication of IMSs (more than 100 made in ≈30 min) coated onto a DVD, with a spatial resolution of 20 μm and thickness of 7.6 μm (**Figure 15**a–b).[141] The laser-scribed interdigitated devices were tested in a PVA/H_2SO_4 gel electrolyte. The capacitance (see **Table 1**, and Figure 15c-d) was proportional to the number of interdigitated electrodes, superior to the capacitance of a device with a sandwich configuration (Figure 4a) and an activated-carbon based device.[141] The high power density was attributed to the open interlayer structure of the electrode and the short ion-diffusion distance between the interdigitated electrodes. The RC constant of the device was 19 ms, which was shorter than that of other carbon-based nanostructures. When using an ionogel (ionic liquid plus fumed silica) as electrolyte, the energy density and power density (see **Table 1**) were further enhanced.[141] The performance of this device was reported to be competitive in energy density with a thin film Li-ion battery and in power density with an aluminum electrolytic capacitor.

3.2.2. *Microsupercapacitors Based on Inorganic 2D Nanomaterials*

Other materials may offer a higher volumetric or areal capacitance compared to pure graphene. MoS_2 nanosheet-based IMSs were prepared by spray coating and laser patterning.[142] They outperformed the rGO-based EDLC microsupercapacitor described above, showing areal capacitance of 8 mF cm^{-2} at 10 mV s^{-1} and volumetric capacitance of 178 F cm^{-3} in 1 M NaOH. This was attributed to redox pseudocapacitance and a crumpled morphology of electrodes that favored electrolyte access.

VS_2 nanosheet-based IMSs were manufactured using a blade-molding technique and were tested in a PVA/BMIM BF_4 gel-ionic liquid electrolyte.[143] Despite the metallic conductivity of VS_2 nanosheets, cyclic voltammetry showed a resistive behavior at 200 mV s^{-1}. The capacitances (coming from only double layer capacitance contribution as no pseudocapacitive activity was identified) reported were 4.7 mF cm^{-2} and 317 F cm^{-3}, but the thickness of the device was only 150 nm.

3.2.3. *Flexible and Free-standing Film Supercapacitors Based on 2D Nanomaterials*

One of the challenges faced in the design of all-solid state supercapacitors is a slow ion transport due to the introduction of a solid or gel electrolyte that has a lower ionic conductivity than a liquid one. An approach to solve this problem is developing an intimate contact between individual particles of active materials and the the solid state electrolyte. A symmetric all-solid state supercapacitor has been manufactured with nafion-functionalized rGO films sandwiching a nafion membrane.[144] Here the nafion polymer was incorporated onto solution exfoliated GO prior to reduction achieving an intimate contact between GO and the polymer. Films were then manufactured by vacuum assisted filtration. The nafion film used as separator was prepared by casting a solution containing H_2SO_4, which increased ionic conductivity, onto the electrode films. This facilitated the incorporation of the electrolyte into the electrode pores. Nafion also served as binder, and a close contact between active material and nafion was aided by hot pressing. All these elements of chemical and manufacturing design resulted in a two-fold increase in capacitance (118.5 F g^{-1} at 1 A g^{-1}) and improved rate performance as compared to a similar device without nafion. The device retained 90 % of capacitance during 1000 cycles under bending conditions showing good mechanical stability.

Wong et al. recently published a study that demonstrated the potential for integration of rGO based devices into wearable electronics.[145] As shown in **Figure 16**a, nickel nanocone arrays (NCA) were electrodeposited onto Ti foils forming a 3D structure, where rGO was electrodeposited. In order to make the device mechanically robust, blocks of ethyl vinyl acetate (EVA) were stencil-printed onto the nickel nanocones array surface prior to rGO electrodeposition. They were uniformly spaced across the electrode area to serve as supports and as separator units. Next, a PVA-Na_2SO_4 gel electrolyte was applied and two such electrodes were assembled face-to-face by hot pressing. A single electrode tested in aqueous Na_2SO_4 electrolyte had a high areal capacitance of 51.3 mF cm^{-2} at 2 mV s^{-1}. The all-solid state symmetric supercapacitor showed an areal capacitance up to 6.84 mF cm^{-2} (Figure 16c), a volumetric capacitance of 1.73 F cm^{-3} for a 45 μm device, a volumetric energy density of 0.15 mWh cm^{-3} and a capacitance retention of 99 % for 20,000 cycles. The relatively high areal capacitance was attributed to

ADVANCED MATERIALS www.advmat.de

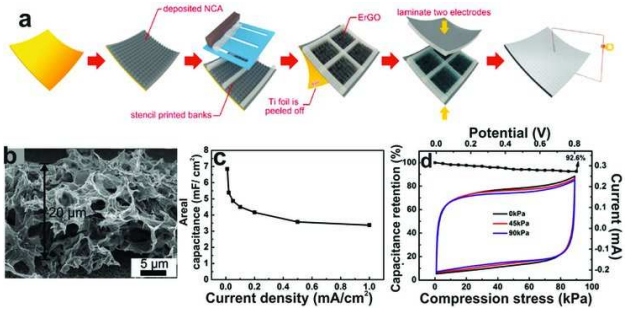

Figure 16. a) Schematic of the manufacture of a tailorable flexible device.[145] Nickel nanocone arrays are electrodeposited onto a Ti foil where EVA "banks" are then stencil-printed. rGO is then electro-deposited and the Ti foil is peeled-off. Two such electrodes are coated with a PVA-Na_2SO_4 gel electrolyte and assembled by hot-pressing, (b) SEM image of the macroporous rGO electrodeposited onto the NCA showing a height of 20 μm, (c) cyclic voltammogram, (d) areal capacitances vs current density curves, (e) capacitance retention vs compression stress curve and cyclic voltammograms under various compression tests. Adapted with permission.[145] Copyright 2015, American Chemical Society.

the enhanced mass loading of active material in the nickel nanocone 3D array as compared to a flat surface, and also due to the macroporous nature of the rGO (Figure 16b). Due to the EVA supports, the device resisted compressive stress up to 90 kPa with 92.6 % capacitance retention (Figure 16d), folding and bending. A connection of 3 supercapacitors in series was capable of lighting a LED during and after cutting with ceramic scissors and while attached to a jacket (both device and cloth were cut). This demonstrated possibility for tailoring and reliability of the device while subject to cutting and puncturing, as required for integration in wearable electronics. However, the weight of metal may be an obstacle to the practical use of this approach.

In another study, hexagonal MnO_2 nanosheets were synthesized using a chemical reduction method and an aqueous MnO_2 nanosheet ink was coated onto conductive multi-walled carbon nanotube paper.[146] The electrode (tested in a half-cell) showed a capacitance of 1,035 F g^{-1} (91.7 mF cm^{-2}) at 2 mV s^{-1}, nearly the theoretical capacitance, in a 0.5 M Na_2SO_4 aqueous electrolyte. A symmetric all-solid state supercapacitor assembled in a sandwich configuration and using a PVA/LiCl gel electrolyte showed a capacitance of 147 F g^{-1} at 2 mV s^{-1}, energy density of 17 Wh kg^{-1} and power density of 38 kW kg^{-1}.[146] Replacing the sandwich configuration by a co-axial geometry, where the MnO_2 coated conductive multiwalled carbon nanotube paper was wrapped around carbon fibers, further enhanced energy density.[146]

3.2.4. Transparent and Flexible Electrodes

The development of transparent supercapacitors is important for flexible, transparent and wearable electronics. For this application, electrodes must meet requirements of high transmittance (> 90 %), low sheet resistance (< 10 Ω sq^{-1}), stretchability and mechanical flexibility.[147] Monolayer or few-layer 2D nanomaterials that are electrically conducting and transparent are particularly promising for this application. Multilayer graphene has been used to manufacture "wrinkled" electrodes with 60 % transparency.[148] An all-solid-state symmetric supercapacitor assembled with these electrodes achieved a capacitance of 6.5 μF cm^{-2} and could be stretched up to 40 % strain without performance degradation over 100 stretching cycles.[148] Other works have combined graphene with metallic nanowire networks in a hybrid with improved transparency and reduced sheet resistance.[149] Materials with electrochromic properties, such as WO_3, are relevant in the development of multifunctional windows that combine energy storage and electrochromism.[150] An electrochromic device made of 2D $WO_3 \cdot 2H_2O$ has shown advantages of more rapid ion diffusion, rapid color switching, and high coloration efficiency, all favored by the high surface area of the nanosheets and the presence of 2D channels.[151] A recent work integrating the electrochromic and pseudocapacitive properties of WO_3 films in a "pseudocapacitive smart window",[150] suggests that this type of multifunctional devices will be greatly improved by using the high-surface-area ultrathin 2D $WO_3 \cdot 2H_2O$.

3.3. 2D and 3D Hybrids Based on 2D Nanomaterials

One of the strategies to impede the stacking of 2D nanomaterials is the introduction of "spacers" in between the nanosheets (Figure 2). These spacers can be other 2D nanomaterials, 0D or 1D nanoparticles or molecules. The resulting hybrid architecture often has an improved performance due to synergistic effects of the components.

IMSs of d-MnO_2/rGO nanosheet hybrids tested in PVA/H_3PO_4 gel electrolyte (**Figure 17**a) showed a better capacitance (250 F g^{-1} at 0.5 A g^{-1}), rate performance (**Figure 17**b), and cyclability (91 % capacitance retention over 7000 cycles) than the graphene-only microsupercapacitors.[28] This was attributed to synergistic effects of the 2D nanomaterials: (i) interleaving of δ−MnO_2 and rGO nanosheets that prevented stacking thus opening up channels for ion transport, and (ii) hybrid interfaces where rGO nanosheets facilitated electronic conduction for an enhanced pseudocapacitive activity of δ−MnO_2 nanosheets. The interdigitated configuration played a key role shortening ion transport distances and promoting transport along the basal plane of the 2D hybrid material. A lower electrical resistance and enhanced electrochemical utilization were favored by a low electrode thickness of only 40 nm, but this certainly limited the total energy stored.

A hybrid of rGO nanosheets and RuO_2 nanoparticles was synthesized using a sol–gel method (**Figure 18**a-b). Oxygen-containing functionalities on the rGO nanosheets favored the anchoring of 5–20 nm RuO_2 nanoparticles.[29] The surface area of the hybrid (281 m^2/g) was larger than the gas accessible surface area of the rGO nanosheets (108 m^2/g), which demonstrated that the nanoparticles acted as spacers. The capacitance of the hybrid with 38 % Ru content was 570 F g^{-1} in a 1 M H_2SO_4 electrolyte, whereas the capacitance of the rGO nanosheets was only 148 F g^{-1}. The measured capacitance of

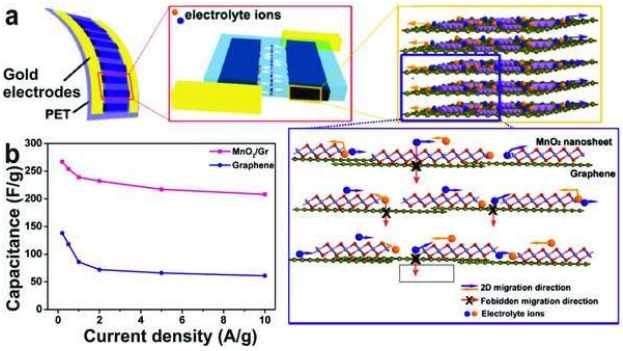

Figure 17. a) Schematic of the δ−MnO_2/rGO nanosheets IMS showing details of the ion transport through 2D channels favored by the interdigitated configuration and the hybrid electrode design,[28] b) capacitance vs current density curve of the δ−MnO_2/rGO nanosheets and rGO-based devices tested in a in PVA/H_3PO_4 gel electrolyte. Reproduced with permission.[28] Copyright 2013, American Chemical Society.

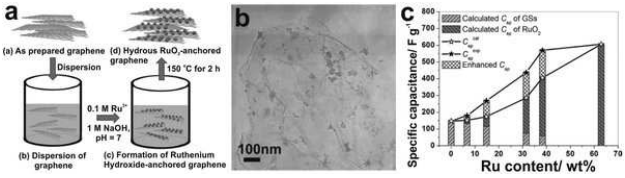

Figure 18. a) Schematic of synthesis of the rGO nanosheets-RuO_2 nanoparticles hybrid showing RuO_2 nanoparticles anchored to rGO,[29] (b) TEM image of the rGO nanosheets-RuO_2 nanoparticles hybrid with 38.3 wt% Ru, (c) capacitance vs Ru content of the rGO nanosheets-RuO_2 nanoparticles hybrid as calculated from cyclic voltammetry at 1 mV s^{-1}. Each bar represents the total measured specific capacitance $C_{sp}^{exp} = C_{sp}^{exp}$ of rGO nanosheets + C_{sp}^{exp} of RuO_2 nanoparticles + a surplus capacitance due to the synergistic effect of the hybrid (grid area). C_{sp}^{calc} indicates calculated specific capacitance.

the hybrid was higher than the calculated from the sum of the contributions of each component, which demonstrated a synergistic effect of the hybridization (Figure 18c). The capacitance of the hybrid was also larger than the capacitance of a mixed composite (360 F g^{-1}). The hybrid had a significantly larger capacitance retention (99.7 %) than RuO_2 powder (42 %) and rGO nanosheets (90.9 %) over a 1,000 cycles stability test.

Synergistic effects were shown by a rGO/MWCNTs IMS tested in a 3 M KCl electrolyte.[152] The hybrid IMS showed a low capacitance (6.1 F cm^{-3} at 10 mV s^{-1}), but was able to perform to the very high scan rate of 50 V s^{-1} retaining 50 % of the capacitance developed at 10 mV s^{-1}. A dramatic capacitance loss (62 % for MWCNTs and 80 % for rGO) was shown by the single-component IMSs. The fast capacitive response of the hybrid IMS was also described by a time constant of 3.4 ms, one order of magnitude lower than the time constant (33 ms) of the rGO-based IMS, and a volumetric power of 77 W cm^{-3}. The improved rate performance of this hybrid device was attributed to the synergistic effects of electrically conducting MWCNTs that acted as nanospacers between rGO nanosheets creating porosity and thus a better accessibility of electrolyte ions, the in-plane and interdigitated design of the device, and the binder-free electrodes.

In a different approach, micrometer-sized films of rGO and polyaniline (PANI) were interleaved to manufacture a rGO/PANI/rGO hybrid free-standing electrode that was tested in 1 M H_2SO_4 electrolyte in a half-cell.[31] The hybrid electrode showed improved capacitance of 581 F g^{-1}, an order of magnitude larger than that of rGO electrode (55 F g^{-1}), and improved cycle stability (85 % capacitance retention over 10,000 cycles). This was attributed to the synergistic effects of redox active PANI sandwiched between rGO sheets having a higher electrical conductivity. The rGO films served as current collectors improving electron transfer to and from PANI while helping to accommodate strain caused by repeated swelling and shrinking of the polymer during cycling.

2D nanomaterials were also used as building blocks of 3D nanostructures. Graphene-based aerogels and hydrogels reviewed in Section 2.1.4 are an example of highly porous and interconnected 3D structures that can be used as binder-free electrodes and scaffolds for pseudocapacitive materials.[26,153] Ball-like 3D rGO crumpled nanostructures are attractive for energy storage due to their porosity, stability against aggregation or deformation either under mechanical stress, heating or solution processing.[154] However, the volumetric characteristics become less impressive as the electrode density decreases. The use of 2D nanomaterials as building blocks of various hybrid structures is discussed in detail elsewhere.[25]

3.4. Printing of Electrodes and Entire Devices

Printing of nanomaterials is a promising technique for the manufacture of flexible devices in a scalable, reproducible and high-throughput manner. Research around the printing of 2D nanomaterials has been focused mostly on rGO, but there are reports on printing of inorganic nanosheets including MoS_2/rGO.[155] rGO has been printed using several techniques including screen printing,[101] inkjet printing,[156] and e-jet printing.[157] A schematic of the inkjet printing technique is presented in **Figure 19**a. Other techniques include a dispensing methodology originally used to manufacture DNA microarrays[158] and micro-extrusion.[159] Screen printing relies on the use of a mask to transfer a pattern onto a substrate,[160] inkjet printing works by ejecting droplets through a nozzle using thermal or acoustic force,[157,161] and e-jet printing is similar to inkjet printing, but it uses an electrical field instead for drop ejection.[157] Most studies focused on improving various critical parameters including adhesion of films to substrates, mechanical stability and flexibility, uniformity of films, printing resolution and good definition of pattern features, ability to produce various electrode patterns, reproducibility, printing speed and scalability.

Inkjet printing is attractive due to its versatility to produce different geometries and designs that can be readily transferred from a computer, reduction of material waste, and ability to print large areas.[162] A particular challenge to inkjet printing

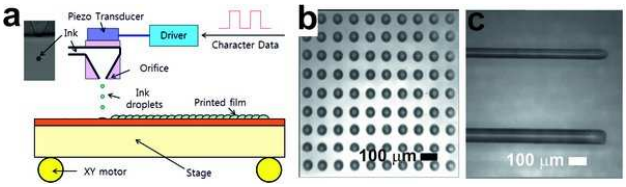

Figure 19. a) Schematic of the inkjet printing process.[161,164] The pattern to print is fed to the system, a driver sends an electrical signal to a piezoelectric print head. In the print head, a piezocrystal expands in response to the electrical driving signal, deforming a membrane, causing a pressure impulse within the ink chamber, and expelling a single droplet from the orifice. The chamber is refilled through the inlet by capillary action at the orifice.[161] The droplets are deposited onto a desired substrate attached to a stage. The stage is displaced by a motor in X and Y directions. In (b) and (c), optical images of graphene patterns printed on glass slides using the terpineol/ethyl cellulose method described in the text.[162] The droplets in (b) are ≈ 55 μm in width and ≈ 50 μm in height. The lines in (c) are are ≈ 60 μm in width and ≈50 μm in height. a) Reproduced with permission. (ECS Transactions 2014, 64 135.) Copyright 2014, The Electrochemical Society. b–c) Reprinted with permission.[162] Copyright 2013 Wiley-VCH.

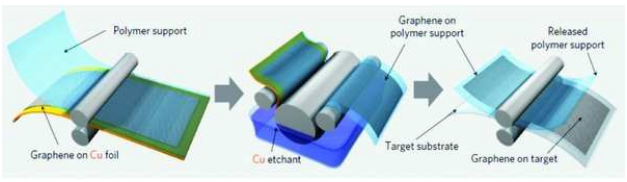

Figure 20. Schematic of the roll-to-roll production of graphene films for transparent electrodes.[165] The process includes adhesion of polymer supports, copper etching (rinsing) and dry transfer-printing on a target substrate. Reproduced with permission.[165] Copyright 2010.

of 2D nanomaterials is the formulation of suitable inks. Particle size of active material that does not clog nozzles, viscosity and surface tension of the carrier liquid, which are required for suitable jet performance, and stability of 2D nanomaterial suspensions, where active materials do not coagulate and separate from the carrier liquid, are critical factors for inkjet printing. A main problem in the printing of graphene is its hydrophobicity that induces agglomeration and destabilization in aqueous suspensions. The viscosity of fluids where graphene is stable, such as DMF and NMP, is not suitable for adequate jet performance.[162] Ostling et al. reported a methodology where graphene is first exfoliated in DMF, this solvent is then replaced by terpineol using distillation, achieving a more concentrated dispersion in a liquid of adequate viscosity for printing (see representative patterns in , **Figure 1**9b-c).[162] The graphene is stabilized against aggregation in terpineol by adding ethyl cellulose prior to distillation. This polymer is then removed by annealing after printing. Another approach for stabilization of graphene dispersions is the use of surfactants such as sodium dodecyl sulfate.[163] These methodologies involve multiple steps and both surfactants and polymers can have a deleterious effect on supercapacitor performance. In fact, most studies reported to date opt for printing graphene oxide first, followed by a post-printing reduction.[156–158]

An important quality metric of a printed pattern is its resolution. Inkjet printing relies mainly on drop size and volume to achieve a given resolution which is controlled by the nozzle size and physical forces involved in drop ejection.[157] The achieved resolution with inkjet printing is 20–30 μm.[157] An improved resolution has been reported for e-jet printing achieving well-defined 5 μm lines.[157] This was attributed to the fact that thinner than the nozzle jets can be produced, enabling a better control over the flow rate and, in turn, to a higher resolution. The drop volume influences drying time and printing time to achieve a desired thickness during printing. E-jet printing can handle drop volumes in the subpicoliter range, which leads to faster drying.[157] Another technique reported for printing a GO-based supercapacitor uses a liquid dispenser, equipment that was originally used for manufacturing DNA arrays.[158] This methodology offers flexibility and control over the dispensed volumes. The minimum volume that could be dispensed in this particular study was 300 pL, which is larger than with e-jet printing. Larger dispensed volumes lead to a larger amount of active material delivered at a time but also longer drying times. Whether this can improve the overall printing time and/or resolution is still to be demonstrated.

3.5. Roll-to-roll Manufacture

The possibility to integrate 2D nanomaterials into large-scale and continuous manufacturing processes has been demonstrated by manufacturing of large-area and flexible graphene films using a roll-to-roll technique. As shown in **Figure 20**, typically, a film of graphene is grown onto a copper foil by CVD, then the graphene film is transferred first to a support film, and then onto a target substrate using the roll-to-roll procedure.[165–167] Ongoing research is focused mainly on optimizing manufacturing variables to achieve uniform films with improved uniform electrical conductivity across large areas and speed of production. A good discussion of the topic can be found elsewhere.[167] These highly conductive graphene films may serve as current collectors for flexible and transparent supercapacitors.

3.6. Optimization of Electrode Density, Thickness and Volumetric Capacitance

The optimization of volumetric and areal capacitance is especially important for microsupercapacitors[77] and devices powering microelectronics where size matters. Unlike, gravimetric capacitance, these metrics account for the entire device including current collector, electrolyte, binder and other components and not only its active component. The gravimetric capacitance takes only the weight of the active material into account and can only be used as a material parameter. The

volumetric capacitance is defined as

$$C_V = \frac{Q}{V \times At}, \quad (5)$$

where Q is charge, V is the voltage window, A and t are area and thickness of the electrode. Equivalently,

$$C_V = C_g \times \rho, \quad (6)$$

where C_g is the gravimetric capacitance and $\rho = m/Vol$ is the electrode density. It is clear from these equations that at a constant electrode area, electrode density and thickness are critical variables for optimization of the volumetric capacitance. In practice, controlling these variables is a manufacturing challenge. Very often as the mass of an electrode increases, the thickness also increases, but the ionic and electronic resistance and the packing density may vary non-uniformly with thickness.[126]

One of the strategies to increase volumetric capacitance is to increase the electrode density. Graphite is the most dense conducting carbon material (2.2 g cm^{-3}) whereas activated carbons incorporating porosity have density of 0.5 to 0.7 g cm^{-3}[[168]] and aerogels possess a much lower density of 0.01-0.1 g cm^{-3}.[72,73] Denser materials allow less accessibility for electrolytes and usually have a low capacitance.[168] For instance, the capacitive performance of dense graphite is poor. On the other hand, low-density carbons that allow easy access of electrolyte are flooded with electrolyte, which produces a net effect of a low volumetric capacitance. The density of graphene varies according to sheet morphology and electrode architecture. The densities of graphene electrodes have been reported to be < 0.5 g cm^{-3}.[77] Flat nanosheets can be tightly packed increasing the electrode density (stacked electrodes), but leading to poor electrolyte access and thus limiting the electrode thickness to a few micrometers or less and leading to underutilization of the material, as many layers are not accessible to electrolyte. Curved and or porous graphene provides a larger gravimetric capacitance but lower electrode densities lead to poor volumetric energy densities.

A clever strategy to manufacture graphene-based electrodes with both improved density and electrolyte access and therefore improved volumetric capacitance has been achieved by incorporating electrolyte in between graphene sheets during electrode manufacturing.[168] Films of chemically reduced rGO were prepared by vacuum assisted filtration. Later, they were soaked on a mix of electrolyte (H_2SO_4 or EMIM BF_4) and water. Once the mix was completely adsorbed on the electrode film, the water was selectively retrieved from the film by vacuum evaporation having the effect of compacting the film and leaving the pre-incorporated electrolyte. SEM images of films with pre-incorporation of H_2SO_4 and different density are shown in **Figure 21**a–b. The density of the electrodes decreased with electrolyte/water fraction pre-incorporated into the films. Symmetric supercapacitors were assembled in a sandwich configuration and tested in 1 M H_2SO_4 or 1 M EMIM BF_4/MeCN electrolytes. The gravimetric capacitance was inversely proportional to electrode density whereas the volumetric capacitance (Figure 21c) was directly proportional to electrode density (255 F cm^{-3} for an electrode of 1.33 g cm^{-3} in 1 M H_2SO_4) and supercapacitors with pre-soaked electrodes had better rate performance than a supercapacitor with completely dry (no electrolyte pre-incorporated) and dense electrodes. The supercapacitor time constant improved with fraction of pre-incorporated electrolyte (0.73 s, electrodes of $\rho = 1.33$ g cm^{-3}) as compared to the dry supercapacitor (3.85 s, electrodes of $\rho = 1.49$ g cm^{-3}). When tested in EMIM BF_4/MeCN, the volumetric energy per unit volume of electrode of a device with dry films decreased dramatically with mass loading (Figure 21d). A less drastic decrease was observed for a device with pre-soaked films (Figures 21d). This showed evidence of an efficient ion transport in pre-soaked films. The Ragone plot in Figure 21e shows the superior performance of pre-soaked devices as compared to dry devices, all tested in EMIM BF_4/ MeCN. A symmetric device with pre-incorporated electrolyte ($\rho = 1.25$ g cm^{-3} and areal mass of 10 mg cm^{-2}) had a stack volumetric energy of 70 Wh L^{-1}. A stack volumetric power of 75 kW L^{-1} was achieved for electrodes with the same density but a lower mass loading of 1.0 mg cm^{-2}. Importantly, this work showed that for the same material, the stack volumetric energy and power densities of a symmetric device are a function of electrode density and mass loading (hence a function of electrode thickness), all important variables to observe when analyzing Ragone plots.[77]

In general, transition metal oxides, hydroxides, dichalcogenides and carbides have a higher specific weight than carbon and can offer a higher volumetric capacitance at the same gravimetric capacitance and a larger areal capacitance at the same film thickness. Therefore, they offer an attractive alternative to graphene for microscale, wearable and transparent energy storage solutions. For instance, MXenes are able to achieve high volumetric capacitances due to their high packing density and ion intercalation capacity. $Ti_3C_2T_x$ as a free-standing paper produced by vacuum assisted filtration had a density of 3.2 g cm^{-3} and achieved a volumetric capacitance of 360 F cm^{-3} (in 1 M Mg_2SO_4).[30] This is larger than the volumetric capacitance achieved by graphene (250-350 F cm^{-3}[[169]]) with much lower packing densities (<0.5 g cm^{-3}). However, the tight architecture of $Ti_3C_2T_x$ paper may hinder electrolyte access and its performance has been improved by intercalating carbon nanotubes in a layer-by-layer fashion resulting in free-standing hybrid films with a density of 2.9 g cm^{-3} that achieved an increase in volumetric capacitance of 300 F cm^{-3}, respect to the non-hybridized $Ti_3C_2T_x$ films.[30] Water and ions pre-intercalated clay-like $Ti_3C_2T_x$ achieved an outstanding volumetric capacitance of 900 F cm^{-3} in 1 M H_2SO_4[126] (see also Section 4.5). A further improvement was achieved by intercalating a redox active polymer between MXene layers.[32] Design of thick electrodes with a high density, but good ion accessibility is the key challenge to improving energy and power density of the devices built of atomically thin 2D sheets.

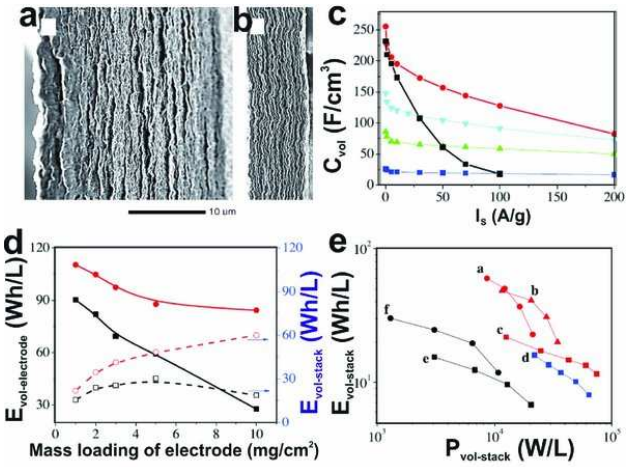

Figure 21. rGO films with pre-incorporated electrolyte and their capacitive performance.[168] SEM images of rGO films pre-incorporated with (a) 78.9 vol % and (b) 27.9 vol % of H_2SO_4 corresponding to densities of 0.42 g cm^{-3} and 1.33 g cm^{-3}, respectively, (c) capacitance per unit volume of electrode vs current rate of symmetric rGO supercapacitors with films pre-incorporated and tested with H_2SO_4 electrolyte and densities of 0.13 g cm^{-3} (blue line), 0.42 g cm^{-3} (green line), 0.76 g cm^{-3} (cyan line), 1.33 g cm^{-3} (red line), and dry films having a density of 1.49 g cm^{-3} (black line), (d) energy per unit volume of electrode and per unit volume of the stacked supercapacitor vs electrode mass loading curves of symmetric supercapacitors of rGO films with (density of 1.25 g cm^{-3}, red lines) and without (density of 1.49 g cm^{-3}, black lines) EMIM BF_4/MeCN electrolyte pre-incorporation that were tested in the same electrolyte at 0.1 A g^{-1}, (e) Ragone plot of supercapacitors with (**a-d**) and without (**e-f**) EMIM BF_4/MeCNelectrolyte pre-incorporation showing the variations of energy and power per unit volume with electrode mass loading and density (**a** 1.25 g cm^{-3}, 10.0 mg cm^{-2}, **b** 1.25 g cm^{-3}, 5.0 mg cm^{-2}, **c** 1.25 g cm^{-3}, 1.0 mg cm^{-2}, **d** 0.39 g cm^{-3}, 1.0 mg cm^{-2}, **e** 1.49 g cm^{-3}, 1.0 mg cm^{-2} and **f** 1.49 g cm^{-3}, 5.0 mg cm^{-2}). Stack volume makes reference to the volume of all the components in a full device. From.[168] Reprinted with permission from AAAS.

4. Challenges and Opportunities

4.1. Low Electrical Conductivity of Some 2D Nanomaterials

The efficient performance of 2D nanomaterials for energy storage is a function of suitable electrochemical activity (double layer or surface redox), electrical conductivity and a surface area accessible to ions. Many 2D nanomaterials have electrochemically active sites that can provide a high capacitance. However, their poor electronic conductivity hinders their electrochemical utilization. As discussed previously, hybridization of semiconducting or insulating oxides with conducting 2D or other low-dimensional nanomaterials is a strategy to improve performance. However, manufacturing procedures of hybrids such as layer-by-layer deposition, vacuum assisted filtration and others have limitations of scalability, efficiency developing suitable nanosheet-nanosheet contacts, and are frequently time-consuming. Physical and chemical modification of poorly conducting 2D nanomaterials to enhance their electrical conductivity is an alternative approach and a comprehensive review of this topic was recently published.[20] Methods to modify the electronic structure of 2D nanomaterials include chemical surface modification, intralayer doping and lattice strain.[20] For instance, the electrical conductivity of TiS_2 has been improved by "injecting" extra electrons in the S-Ti-S lattice by functionalizing it with hydrogen.[170] Films of H_yTiS_2 nanosheets achieved an electrical conductivity of 6.76×10^4 S m^{-1} at 298 K. For comparison, the reported conductivity of indium tin oxide transparent films is 1.9×10^4 S m^{-1}[171] and 1.4×10^5 S m^{-1}[172]. The change of semiconducting behavior of 2H-MoS_2 to metallically conducting 1T-MoS_2 has been achieved by chemically intercalating Li- or Na-ions[173] that reduce the Mo atoms inducing a transition from prismatic to octahedral coordination, d-orbital splitting and rearrangement of orbital filling.[18,123,174] This increase in electrical conductivity leads to an increase in capacitance and energy density of MoS_2 electrodes. Partial reduction and formation of oxygen deficient structures may significantly increase electronic conductivity of transition metal oxides.[175] Understanding of the electrical properties of 2D nanomaterials, their change as a result of coupling with a material having a different work function, effects of surface termination, defects, electrolyte adsorption and other factors should allow suitable tuning and tailoring for supercapacitor applications.

4.2. Chemical and Electrochemical Instability

Among the drawbacks of several 2D nanomaterials is their chemical and/or electrochemical instability. Metal oxides are more stable than sulfides, carbides and nitrides. TMDs such as TiS_2 are particularly sensitive to oxidation in air and moisturized environments[176] and therefore unsuitable for symmetric aqueous supercapacitors. H-MoS_2 has shown poor cycle stability and this has been mainly attributed to its semiconducting nature.[6] This poor performance has been alleviated by hybridization with graphene[177] or other carbon-based materials[178] that provide electrical conductivity and mechanical robustness. T-MoS_2 with a metallic character has shown an improved cycle stability in aqueous electrolytes.[18] In this sense, MXenes offer advantages of intrinsic metallic conductivity and their cycle stability has been demonstrated up to 10,000 cycles.[126] However, they can be oxidized by oxygen dissolved in the electrolyte or when a high anodic potential is applied in an aqueous electrolyte.[11,179] In the case of activated graphene, the presence of oxygen-containing chemical functionalities is known to lead to poorer cycle stability that can be alleviated by annealing.[56]

4.3. Electrolytes and Electrode-Electrolyte Interfaces

The energy density of nanomaterials can be improved by enlarging the voltage window (Equations 2 and3).[12] Higher energy densities are achieved by moving from 0.9-1.0 V for symmetric devices in aqueous electrolytes to 1–2 V for hybrid de-

vices, 2.5–2.7 V for supercapacitors with organic electrolytes, and to 3–4 V for devices using ionic liquids.[12,180] There are relatively few reports on the capacitive performance of 2D nanomaterials in nonaqueous electrolytes due to slow transport of large organic ions in narrow slit pores between 2D sheets.[136] Also, the pseudocapacitive charge storage mechanism that is responsible for energy storage in oxides, chalcogenides and carbides of transition metals may not work in organic electrolytes. Protic ionic liquids or Li^+ containing electrolytes may provide a solution. Activated MEGO and 1T-MoS_2 have shown enhanced energy density when using organic electrolytes or ionic liquids.[18,23] The largest capacitance and energy density of activated MEGO was found when using BMIM BF_4/MeCN (3.5 V).[23] By using a suitable mix of ionic liquids, activated MEGO delivered a much higher capacitance (up to 170 F g^{-1}) compared to carbon nanotubes and carbon onions in a wide temperature range of -50 to 80 °C.[56] Similarly, a larger volumetric energy density was found for 1T-MoS_2 when using TEA-BF_4/MeCN and BMIM-BF_4/MeCN.[18]

Electrolyte choice is intrinsically linked to the design of electrode-electrolyte interfaces. The properties of the 2D nanomaterial surface determine the nature of the interaction with specific electrolytes and include: (i) hydrophilicity or hydrophobicity (ionophobicity), (ii) presence of functional groups on the surface and their nature, (iii) porosity and pore size, and (iv) specific surface area accessible to electrolyte ions. Besides nanosheet surface properties, the spacing between nanosheets, nanosheet morphology and arrangement in electrode films determine their intercalation ability, ion transport properties and energy storage mechanisms. For instance, the ability of multilayered $Ti_3C_2T_x$ to simultaneously show high energy and power densities in acidic electrolytes, i.e., fast rate performance, was attributed to adsorption of protons onto $Ti_3C_2T_x$ layers and fast charge transfer to Ti atoms in the outer Ti layer.[13] A dynamic access of protons and other cations into the MXene galleries was enabled by the presence of water molecules and ions prior to electrochemical intercalation into multi-layered $Ti_3C_2T_x$.[13] Completely delaminated $Ti_3C_2T_x$ improved capacitance and rate response even more due to its higher surface area available for ion adsorption and enhanced mechanical flexibility.[13] The presence of water molecules in the inter-layer space has also been associated with the charge storage mechanisms undergone by 1T MoS_2 in various aqueous electrolytes.[18]

These findings clearly point towards research venues in 2D nanomaterials that embrace the design of morphology and texture of active materials, study of electrode-electrolyte interfaces, finding an appropriate electrolyte, and study of energy storage mechanisms as a means to improve supercapacitor performance. Finding nonaqueous electrolytes that enable pseudocapacitive energy storage in a variety of transition metal containing compounds may lead to a major breakthrough in energy storage.

4.4. Synthesis Methods and Control of Nanosheet Size and Thickness

Control of size and thickness of 2D nanomaterials remains to be a synthesis challenge. As compared to multi-layer materials, single-layer nanosheets provide an enhanced specific surface area, a larger number of sites for pseudocapacitive activity, and a faster ion transport through inter-sheet spaces, provided that re-stacking has been mitigated. Supporting this argument, it has been found that the volumetric capacitance of h-MoO_3 nanosheets decreases as the nanosheet thickness is increased from 1.6 nm to 12 nm.[111] A larger nanosheet lateral size is expected to enhance electrical conductivity as there will be fewer nanosheet-nanosheet contacts,[111] but it can also hinder diffusion of ions and decrease the charge/discharge rate. In addition, the materials surface must be free of contaminations, such as surfactant or polymeric binders, which will reduce active surface area while preventing adequate electrode-electrolyte contact. Liquid-phase exfoliation methods can produce mostly few-layer nanosheets with lateral dimensions of at most a few micrometers.[42] Environmentally friendly solvents but less effective for liquid-phase exfoliation produce preferentially multilayered "nanosheets",[109] or nanoplatelets.[181] If surfactants are used, a post-synthesis removal step is necessary.[43] Methods using intercalation of bulky organic ions to induce exfoliation usually produce nanosheets of lateral dimension in the submicrometer range,[98–100] have problems of contamination with intercalant residues, and may lead to a high fraction of non-delaminated material.[98] The latter can usually be separated by centrifugation. Chemical and electrochemical lithiation followed by ultrasonication in water has proved to be effective in producing single-layer TMDs.[6,18,123] However, residuals of lithiation compounds may remain as contamination. CVD methods produce high-quality and large-size single-layer nanosheets, but generally with a low yield.[182] A new method to produce large-area metal oxides including MoO_3, WO_3, MoO_2 and MnO uses salts as template to guide the growth of crystals at high temperatures and in vacuum.[111] This method allows the synthesis of nanosheets of non-layered metal oxides that cannot be produced by exfoliation methods that rely on precursors with a layered crystal structure that can be cleaved through weak bonds.

4.5. Scale-up of Thin Films Manufacturing

Volumetric capacitance, hence energy per unit volume, deteriorates as electrode thickness increases due to mass transport limitations and increase of electrode resistance. This effect becomes more pronounced when the overall device volume is considered.[77] In addition, the variation of volumetric capacitance with electrode thickness is not linear.[168] Thin films with a high volumetric capacitance but a small amount of energy stored may be suitable for microsupercapacitors. Most studies in 2D nanomaterials have been carried out with thin films with at most few-micrometers thickness, and thus are considered suitable for micro-supercapacitor applications. New frontiers for supercapacitor applications demanding large energy densities may be opened by new and newly designed 2D nanomaterials. MXenes, for instance, can provide high volumetric capacitances with fairly thick electrodes; clay-like $Ti_3C_2T_x$ showed volumetric capacitances of ≈550 F cm^{-3} and ≈380 F cm^{-3} for electrodes with thicknesses of 30 μm and 75 μm, respectively.[126]

4.6. Scalability of Synthesis and Electrode Manufacturing

Scaling-up current 2D nanomaterials synthesis methods and devising new scalable and inexpensive manufacturing methods is a concern for the realization of commercial applications which require large quantities (tons) and high throughput production.[183] In the context of supercapacitor applications, activation processes and synthesis of exfoliated and reduced graphene oxide offer a potential for scalability.[23] Scale-up in the production of graphene by liquid-phase exfoliation has been demonstrated.[41] This suggests that scale-up can be extended to TMDs produced by the same method. However, further improvement of yield of liquid-phase exfoliation methods is necessary to meet the needs of industry.[183] The areal scalability of CVD methods has been demonstrated by the roll-to-roll production of graphene films.[165–167] Proposed methods for the synthesis of existent or new 2D nanomaterials need to be scalable, to reach at least the volumes required for electronic applications.

The scalability of electrode manufacturing is at an early stage and a demonstration has been given by the high throughput fabrication of rGO microsupercapacitors (100 devices /30 min) using laser scribing.[141] Many of the currently used laboratory techniques such as layer-by-layer deposition by dip coating or vacuum assisted filtration have a limited potential for large-volume manufacturing. 2D and 3D printing and spray-deposition are promising techniques for the large-scale manufacturing of film electrodes,[43] as well as hybrid 2D[27] and 3D hierarchical structures.

5. Summary and Outlook

The application of 2D nanomaterials in supercapacitors is a hot research area. First graphene and then a series of 2D inorganic nanomaterials were investigated and have demonstrated a potential in various energy storage applications. Due to their 2D nature that provides a high surface area accessible to ions, the availability of multiple reaction sites and inter-layer spaces, and the possibility to modify their surface chemistry, 2D nanomaterials can store energy by electrical double layer capacitance, redox and ion intercalation pseudocapacitance.

Nanosheet composition, shape, texture, thickness and electrode architecture play a crucial role in energy storage. Studies on graphene-based and inorganic 2D nanomaterials showed that the optimum energy storage is achieved with porous and curved nanosheets that allow fast ion transport through 2D channels and across nanosheets. New findings show the role of quantum capacitance in the energy storage of graphene based and related materials. The capacitance of inorganic 2D nanomaterials including h-MoO_3 was found to decrease with increasing nanosheet thickness. This showed that single-layer nanosheets can maximize energy storage. In-plane electrode geometry with interdigitated electrodes favored an enhanced storage and faster ion transport compared to the traditional sandwich device architecture.

Drawbacks of 2D nanomaterials, such as poor electrical conductivity of many of them and a tendency to re-stack that limits ion transport, have been tackled through hybridization. Synergistic effects resulting in enhanced capacitance, rate performance and cycling stability have been observed between graphene and 2D metal oxide nanoparticles, carbon nanotubes and polymers. Doped graphene-based aerogels and MXenes offered the possibility to manufacture binder-free and mechanically strong electrodes with enhanced capacitances. Aerogels were also used as scaffolds for other nanomaterials with pseudocapacitive properties, further enhancing the overall energy storage. The design of 3D hierarchical structures combining 2D nanomaterials with other nanomaterials has shown to add up greatly to enhancement of energy storage.

2D nanomaterials have been exploited for the manufacture of flexible, free-standing and binder free supercapacitors, all-solid-state supercapacitors, and microsupercapacitors. Major achievements have been realized in the fabrication of flexible rGO microsupercapacitors. The potential of 2D nanomaterials-based supercapacitors to be integrated into wearable electronics has been demonstrated with an rGO-based all solid state supercapacitor that tolerated bending, puncturing and cutting while performing well in terms of energy storage.

Due to their high packing density, 2D nanomaterials are particularly promising in the development of miniaturized devices with high volumetric and areal capacitances. High packing density, however, may impede electrolyte access to the active surface of nanosheets. This problem has been tackled by pre-incorporating electrolytes in between nanosheets (wetting) or pillaring with large molecules prior to electrode manufacturing. This approach has also been applied to solid (gel) electrolytes to enhance ionic conductivity through the bulk of the electrode. Pre-intercalation of water and ions in between 2D nanosheets has been found to play a key role in utilizing the full energy storage potential of MXenes and 1T-MoS_2 by facilitating ion intercalation and fast and reversible ion adsorption when tested in aqueous electrolytes.

In order to fully utilize the available electrochemically active sites of poorly conducting 2D nanomaterials, research efforts are focused on improving their intrinsic electrical conductivity. Methods that modify the electronic structure of 2D nanomaterials include partial reduction of oxides, chemical surface modification, intralayer doping and lattice strain. Their efficiency has been demonstrated, for instance, by improving the electrical conductivity of metal dichalcogenides. These findings and appreciation of the role of quantum capacitance emphasize the importance of understanding the fundamental properties of 2D nanomaterials to be in a position to fully exploit them in energy storage applications.

Many challenges still remain for the wide use of 2D nanomaterials in energy storage. Chemical and/or electrochemical instability of some 2D nanomaterials is a main drawback. Many of the emerging new 2D nanomaterials, such as phosphorene,[184] and silicene[185] are unstable an air. Insulating materials, such as boronitrene[186] can only be used in separators. Some other materials are difficult to synthesize[185] and are unavailable in amounts required for supercapacitor applications. Even MXenes oxidize easily under anodic potential in aqueous electrolytes, requiring coupling with more stable positive electrodes in hybrid devices. The investigation and/or design of new 2D nanomaterials must take into account their stability along with

compatibility with suitable electrolytes in wide electrochemical windows that enable an enhanced energy density, and the design of suitable electrode-electrolyte interfaces.

Synthesis methods must improve control of nanosheet thickness and size, yield, minimize the content of contaminants in the final product, while offering reproducibility, scalability, being environmentally friendly and cost effective. Currently, the cost involved in the synthesis of 2D nanomaterials using sophisticated methods and/or exotic and expensive precursors is much higher than that of producing conventional activated carbon powders used in the majority of supercapacitors today. The scalability of manufacturing 2D nanomaterials-based electrodes has been demonstrated for graphene.[141] Printing of 2D nanomaterials is promising and current research is seeking to improve composition of inks, printing speed and resolution. A significant progress in the application of 2D nanomaterials in supercapacitors has been made. Findings described here point to clear research venues that should lead to further progress in the future.

Acknowledgements

Y.G. was supported by the Fluid Interface Reactions, Structures and Transport (FIRST) Center, an Energy Frontier Research Center funded by the U.S. Department of Energy, Office of Science, and Office of Basic Energy Sciences. The authors thank Tyler Mathis (Drexel University) for helpful comments on the manuscript.

Received: December 9, 2015
Revised: February 15, 2016
Published Online: MM DD, YYYY

[1] Z. Yu, L. Tetard, L. Zhai, J. Thomas, *Energy Environ. Sci.* **2015**, *8*, 702.
[2] S. Z. Butler, S. M. Hollen, L. Cao, Y. Cui, J. A. Gupta, H. R. Gutiérrez, T. F. Heinz, S. S. Hong, J. Huang, A. F. Ismach, E. Johnston-Halperin, M. Kuno, V. V. Plashnitsa, R. D. Robinson, R. S. Ruoff, S. Salahuddin, J. Shan, L. Shi, M. G. Spencer, M. Terrones, W. Windl, J. E. Goldberger, *ACS Nano* **2013**, *7*, 2898.
[3] Y. Gogotsi, *ACS Nano* **2014**, *8*, 5369.
[4] M. D. Stoller, S. Park, Y. Zhu, J. An, R. S. Ruoff, *Nano Lett.* **2008**, *8*, 3498.
[5] X. Peng, L. Peng, C. Wu, Y. Xie, *Chem. Soc. Rev.* **2014**, *43*, 3303.
[6] M. Chhowalla, H. S. Shin, G. Eda, L.-J. Li, K. P. Loh, H. Zhang, *Nat. Chem.* **2013**, *5*, 263.
[7] M. Naguib, O. Mashtalir, J. Carle, V. Presser, J. Lu, L. Hultman, Y. Gogotsi, M. W. Barsoum, *ACS Nano* **2012**, *6*, 1322.
[8] M. Naguib, G. W. Bentzel, J. Shah, J. Halim, E. N. Caspi, J. Lu, L. Hultman, M. W. Barsoum, *Mater. Res. Lett.* **2014**, *2*, 233.
[9] M. Naguib, M. Kurtoglu, V. Presser, J. Lu, J. Niu, M. Heon, L. Hultman, Y. Gogotsi, M. W. Barsoum, *Adv. Mater.* **2011**, *23*, 4248.
[10] M. Naguib, V. N. Mochalin, M. W. Barsoum, Y. Gogotsi, *Adv. Mater.* **2014**, *26*, 992.
[11] M. R. Lukatskaya, O. Mashtalir, C. E. Ren, Y. Dall'Agnese, P. Rozier, P. L. Taberna, M. Naguib, P. Simon, M. W. Barsoum, Y. Gogotsi, *Science* **2013**, *341*, 1502.
[12] P. Simon, Y. Gogotsi, *Nat. Mater.* **2008**, *7*, 845.
[13] M. D. Levi, M. R. Lukatskaya, S. Sigalov, M. Beidaghi, N. Shpigel, L. Daikhin, D. Aurbach, M. W. Barsoum, Y. Gogotsi, *Adv. Energy Mater.* **2015**, *5*, 1400815.
[14] M. Beidaghi, Y. Gogotsi, *Energy Environ. Sci.* **2014**, *7*, 867.
[15] A. K. Geim, K. S. Novoselov, *Nat. Mater.* **2007**, *6*, 183.
[16] a) K. S. Novoselov, A. K. Geim, S. V. Morozov, D. Jiang, M. I. Katsnelson, I. V. Grigorieva, S. V. Dubonos, A. A. Firsov, *Nature* **2005**, *438*, 197; b) K. S. Novoselov, A. K. Geim, S. V. Morozov, D. Jiang, Y. Zhang, S. V. Dubonos, I. V. Grigorieva, A. A. Firsov, *Science* **2004**, *306*, 666; c) S. Pisana, M. Lazzeri, C. Casiraghi, K. S. Novoselov, A. K. Geim, A. C. Ferrari, F. Mauri, *Nat. Mater.* **2007**, *6*, 198.
[17] Z. Ling, C. E. Ren, M.-Q. Zhao, J. Yang, J. M. Giammarco, J. Qiu, M. W. Barsoum, Y. Gogotsi, *Proc. Natl. Acad. Sci. US A* **2014**, *111*, 16676.
[18] M. Acerce, D. Voiry, M. Chhowalla, *Nat. Nanotechnol.* **2015**, *10*, 313.
[19] K. F. Mak, C. Lee, J. Hone, J. Shan, T. F. Heinz, *Phys. Rev. Lett.* **2010**, *105*, 136805.
[20] F. Feng, J. Wu, C. Wu, Y. Xie, *Small* **2015**, *11*, 654.
[21] a) J. Wang, B. Ding, Y. Xu, L. Shen, H. Dou, X. Zhang, *ACS Appl. Mater. Interfaces* **2015**, *7*, 22284; b) J. Zang, C. Cao, Y. Feng, J. Liu, X. Zhao, *Sci. Rep.* **2014**, *4*, 6492.
[22] J. R. Miller, R. A. Outlaw, B. C. Holloway, *Science* **2010**, *329*, 1637.
[23] Y. Zhu, S. Murali, M. D. Stoller, K. J. Ganesh, W. Cai, P. J. Ferreira, A. Pirkle, R. M. Wallace, K. A. Cychosz, M. Thommes, D. Su, E. A. Stach, R. S. Ruoff, *Science* **2011**, *332*, 1537.
[24] X. Zhao, C. M. Hayner, M. C. Kung, H. H. Kung, *ACS Nano* **2011**, *5*, 8739.
[25] J. L. Gunjakar, I. Y. Kim, J. M. Lee, Y. K. Jo, S.-J. Hwang, *J. Phys. Chem. C* **2014**, *118*, 3847.
[26] a) Z. Tang, S. Shen, J. Zhuang, X. Wang, *Angew. Chem. Int. Ed.* **2010**, *49*, 4603; b) W. Chen, S. Li, C. Chen, L. Yan, *Adv. Mater.* **2011**, *23*, 5679.
[27] B. Mendoza-Sánchez, J. Coelho, A. Pokle, V. Nicolosi, *Electrochim. Acta* **2015**, *174*, 696.
[28] L. Peng, X. Peng, B. Liu, C. Wu, Y. Xie, G. Yu, *Nano Lett.* **2013**, *13*, 2151.
[29] Z.-S. Wu, D.-W. Wang, W. Ren, J. Zhao, G. Zhou, F. Li, H.-M. Cheng, *Adv. Funct. Mater.* **2010**, *20*, 3595.
[30] M.-Q. Zhao, C. E. Ren, Z. Ling, M. R. Lukatskaya, C.-F. Zhang, K. L. V. Aken, M. Barsoum, Y. Gogotsi, *Adv. Mater.* **2015**, *5*, 1401286.
[31] F. Xiao, S. Yang, Z. Zhang, H. Liu, J. Xiao, L. Wan, J. Luo, S. Wang, Y. Liu, *Sci. Rep.* **2015**, *5*, 9359.
[32] M. Boota, B. Anasori, C. Voigt, M.-Q. Zhao, M. W. Barsoum, Y. Gogotsi, *Adv. Mater.* **2015**.
[33] a) H. Wang, H. Feng, J. Li, *Small* **2014**, *10*, 2165; b) X. Huang, Z. Zeng, H. Zhang, *Chem. Soc. Rev.* **2013**, *42*, 1934.
[34] Y. Zhang, Y.-W. Tan, H. L. Stormer, P. Kim, *Nature* **2005**, *438*, 201.
[35] a) K. S. Subrahmanyam, S. R. C. Vivekchand, A. Govindaraj, C. N. R. Rao, *J. Mater. Chem.* **2008**, *18*, 1517; b) S. R. C. Vivekchand, C. Rout, K. S. Subrahmanyam, A. Govindaraj, C. N. R. Rao, *J. Chem. Sci.* **2008**, *120*, 9.
[36] a) R. Mas-Balleste, C. Gomez-Navarro, J. Gomez-Herrero, F. Zamora, *Nanoscale* **2011**, *3*, 20; b) C. N. R. Rao, A. K. Sood, *Graphene, Synthesis, Properties, and Phenomena*, Wiley-VCH, Weinheim, Germany **2013**; c) P. Avouris, C. Dimi-

trakopoulos, *Mater. Today* **2012**, *15*, 86; d) Y. Zhu, S. Murali, W. Cai, X. Li, J. W. Suk, J. R. Potts, R. S. Ruoff, *Adv. Mater.* **2010**, *22*, 3906.
[37] V. Singh, D. Joung, L. Zhai, S. Das, S. I. Khondaker, S. Seal, *Prog. Mater Sci.* **2011**, *56*, 1178.
[38] X. Huang, Z. Yin, S. Wu, X. Qi, Q. He, Q. Zhang, Q. Yan, F. Boey, H. Zhang, *Small* **2011**, *7*, 1876.
[39] M. Terrones, A. R. Botello-Méndez, J. Campos-Delgado, F. López-Urías, Y. I. Vega-Cantú, F. J. Rodríguez-Macías, A. L. Elías, E. Muñoz-Sandoval, A. G. Cano-Márquez, J.-C. Charlier, H. Terrones, *Nano Today* **2010**, *5*, 351.
[40] A. Bianco, H.-M. Cheng, T. Enoki, Y. Gogotsi, R. H. Hurt, N. Koratkar, T. Kyotani, M. Monthioux, C. R. Park, J. M. D. Tascon, J. Zhang, *Carbon* **2013**, *65*, 1.
[41] K. R. Paton, E. Varrla, C. Backes, R. J. Smith, U. Khan, A. O'Neill, C. Boland, M. Lotya, O. M. Istrate, P. King, T. Higgins, S. Barwich, P. May, P. Puczkarski, I. Ahmed, M. Moebius, H. Pettersson, E. Long, J. Coelho, S. E. O'Brien, E. K. McGuire, B. M. Sanchez, G. S. Duesberg, N. McEvoy, T. J. Pennycook, C. Downing, A. Crossley, V. Nicolosi, J. N. Coleman, *Nat. Mater.* **2014**, *13*, 624.
[42] Y. Hernandez, V. Nicolosi, M. Lotya, F. M. Blighe, Z. Sun, S. De, I. T. McGovern, B. Holland, M. Byrne, Y. K. Gun'Ko, J. J. Boland, P. Niraj, G. Duesberg, S. Krishnamurthy, R. Goodhue, J. Hutchison, V. Scardaci, A. C. Ferrari, J. N. Coleman, *Nat. Nanotechnol.* **2008**, *3*, 563.
[43] B. Mendoza-Sánchez, B. Rasche, V. Nicolosi, P. S. Grant, *Carbon* **2013**, *52*, 337.
[44] M. Lotya, P. J. King, U. Khan, S. De, J. N. Coleman, *ACS Nano* **2010**, *4*, 3155.
[45] J. J. Yoo, K. Balakrishnan, J. Huang, V. Meunier, B. G. Sumpter, A. Srivastava, M. Conway, A. L. Mohana Reddy, J. Yu, R. Vajtai, P. M. Ajayan, *Nano Lett.* **2011**, *11*, 1423.
[46] J. P. Randin, E. Yeager, *J. Electrochem. Soc.* **1971**, *118*, 711.
[47] X. Zhao, H. Tian, M. Zhu, K. Tian, J. J. Wang, F. Kang, R. A. Outlaw, *J. Power Sources* **2009**, *194*, 1208.
[48] S. Stankovich, D. A. Dikin, R. D. Piner, K. A. Kohlhaas, A. Kleinhammes, Y. Jia, Y. Wu, S. T. Nguyen, R. S. Ruoff, *Carbon* **2007**, *45*, 1558.
[49] M. D. Stoller, S. J. Park, Y. W. Zhu, J. H. An, R. S. Ruoff, *Nano Lett.* **2008**, *8*, 3498.
[50] K. Haubner, J. Murawski, P. Olk, L. M. Eng, C. Ziegler, B. Adolphi, E. Jaehne, *ChemPhysChem* **2010**, *11*, 2131.
[51] H. Hu, Z. Zhao, Q. Zhou, Y. Gogotsi, J. Qiu, *Carbon* **2012**, *50*, 3267.
[52] Y. Zhu, S. Murali, M. D. Stoller, A. Velamakanni, R. D. Piner, R. S. Ruoff, *Carbon* **2010**, *48*, 2118.
[53] Y. Wang, Z. Shi, Y. Huang, Y. Ma, C. Wang, M. Chen, Y. Chen, *J. Phys. Chem. C* **2009**, *113*, 13103.
[54] W. Lv, D.-M. Tang, Y.-B. He, C.-H. You, Z.-Q. Shi, X.-C. Chen, C.-M. Chen, P.-X. Hou, C. Liu, Q.-H. Yang, *ACS Nano* **2009**, *3*, 3730.
[55] L. L. Zhang, X. Zhao, M. D. Stoller, Y. Zhu, H. Ji, S. Murali, Y. Wu, S. Perales, B. Clevenger, R. S. Ruoff, *Nano Lett.* **2012**, *12*, 1806.
[56] W.-Y. Tsai, R. Lin, S. Murali, L. Li Zhang, J. K. McDonough, R. S. Ruoff, P.-L. Taberna, Y. Gogotsi, P. Simon, *Nano Energy* **2013**, *2*, 403.
[57] K. Jost, **Figure**. Ion electrosorption on an activated graphene electrode, *2D Materials, Focus on the Applications of Graphene for Energy Storage* **2015**.
[58] C. Portet, G. Yushin, Y. Gogotsi, *Carbon* **2007**, *45*, 2511.
[59] V. Presser, L. Zhang, J. J. Niu, J. McDonough, C. Perez, H. Fong, Y. Gogotsi, *Adv. Energy Mater.* **2011**, *1*, 423.
[60] J. Chmiola, G. Yushin, Y. Gogotsi, C. Portet, P. Simon, P. L. Taberna, *Science* **2006**, *313*, 1760.
[61] D. Wei, Y. Liu, Y. Wang, H. Zhang, L. Huang, G. Yu, *Nano Lett.* **2009**, *9*, 1752.
[62] Z. Jin, J. Yao, C. Kittrell, J. M. Tour, *ACS Nano* **2011**, *5*, 4112.
[63] H. Nolan, B. Mendoza-Sanchez, N. Ashok Kumar, N. McEvoy, S. O'Brien, V. Nicolosi, G. S. Duesberg, *Phys. Chem. Chem. Phys.* **2014**, *16*, 2280.
[64] H. M. Jeong, J. W. Lee, W. H. Shin, Y. J. Choi, H. J. Shin, J. K. Kang, J. W. Choi, *Nano Lett.* **2011**, *11*, 2472.
[65] Y.-C. Lin, C.-Y. Lin, P.-W. Chiu, *Appl. Phys. Lett.* **2010**, *96*, 133110.
[66] Z. Wen, X. Wang, S. Mao, Z. Bo, H. Kim, S. Cui, G. Lu, X. Feng, J. Chen, *Adv. Mater.* **2012**, *24*, 5610.
[67] Y. Zou, I. A. Kinloch, R. A. W. Dryfe, *J. Mater. Chem. A* **2014**, *2*, 19495.
[68] J. W. Lee, J. M. Ko, J.-D. Kim, *Electrochim. Acta* **2012**, *85*, 459.
[69] S. V. Savilov, E. A. Arkhipova, A. S. Ivanov, K. I. Maslakov, Z. Shen, S. M. Aldoshin, V. V. Lunin, *Mater. Res. Bull.* **2015**, *69*, 7.
[70] Y. Xu, K. Sheng, C. Li, G. Shi, *ACS Nano* **2010**, *4*, 4324.
[71] a) Z. Zhao, T. Mei, Y. Chen, J. Qiu, D. Xu, J. Wang, J. Li, X. Wang, *Mater. Res. Bull.* **2015**, *68*, 245; b) P. Chen, J.-J. Yang, S.-S. Li, Z. Wang, T.-Y. Xiao, Y.-H. Qian, S.-H. Yu, *Nano Energy* **2013**, *2*, 249.
[72] X. Zhang, Z. Sui, B. Xu, S. Yue, Y. Luo, W. Zhan, B. Liu, *J. Mater. Chem.* **2011**, *21*, 6494.
[73] M. A. Worsley, P. J. Pauzauskie, T. Y. Olson, J. Biener, J. H. Satcher, T. F. Baumann, *J. Am. Chem. Soc.* **2010**, *132*, 14067.
[74] S. De, P. J. King, M. Lotya, A. O'Neill, E. M. Doherty, Y. Hernandez, G. S. Duesberg, J. N. Coleman, *Small* **2010**, *6*, 458.
[75] Z.-S. Wu, A. Winter, L. Chen, Y. Sun, A. Turchanin, X. Feng, K. Müllen, *Adv. Mater.* **2012**, *24*, 5130.
[76] T. Wang, L.-X. Wang, D.-L. Wu, W. Xia, D.-Z. Jia, *Sci. Rep.* **2015**, *5*, 9591.
[77] Y. Gogotsi, P. Simon, *Science* **2011**, *334*, 917.
[78] a) Y. E. Lozovik, A. A. Sokolik, A. D. Zabolotskiy, *Phys. Rev. B: Condens. Matter Mater. Phys.* **2015**, *91*, 075416; b) E. Paek, A. J. Pak, G. S. Hwang, *J. Chem. Phys.* **2015**, *142*, 024701; c) S. Dröscher, P. Roulleau, F. Molitor, P. Studerus, C. Stampfer, K. Ensslin, T. Ihn, *Appl. Phys. Lett.* **2010**, *96*, 152104.
[79] D. Bischoff, M. Eich, A. Varlet, P. Simonet, T. Ihn, K. Ensslin, *Phys. Rev. B: Condens. Matter Mater. Phys.* **2015**, *91*, 115441.
[80] L. L. Zhang, X. Zhao, H. Ji, M. D. Stoller, L. Lai, S. Murali, S. McDonnell, B. Cleveger, R. M. Wallace, R. S. Ruoff, *Energy Environ. Sci.* **2012**, *5*, 9618.
[81] H. Ji, X. Zhao, Z. Qiao, J. Jung, Y. Zhu, Y. Lu, L. L. Zhang, A. H. MacDonald, R. S. Ruoff, *Nat. Commun.* **2014**, 5.
[82] J. Xia, F. Chen, J. Li, N. Tao, *Nat. Nanotechnol.* **2009**, *4*, 505.
[83] J. Martin, N. Akerman, G. Ulbricht, T. LOhmann, J. H. Smet, K. von Klitzing, A. Yacoby, *Nat. Phys.* **2008**, *4*, 144.
[84] B. Dyatkin, Y. Gogotsi, *Faraday Discuss.* **2014**, *172*, 139.
[85] J. Chmiola, C. Largeot, P. L. Taberna, P. Simon, Y. Gogotsi, *Angew. Chem. Int. Ed.* **2008**, *47*, 3392.
[86] C. Largeot, C. Portet, J. Chmiola, P. L. Taberna, Y. Gogotsi, P. Simon, *J. Am. Chem. Soc.* **2008**, *130*, 2730.
[87] a) H. Huang, B. G. Sumpter, V. Meunier, *Angew. Chem. Int. Ed.* **2008**, *47*, 520; b) J. Huang, B. G. Sumpter, V. Meunier, *Chem. - Eur. J.* **2008**, *14*, 6614.
[88] Y. Qiu, Y. Chen, *J. Phys. Chem. C* **2015**, *119*, 23813.
[89] J. J. Lin, S. M. Huang, Y. H. Lin, T. C. Lee, H. Liu, X. X. Zhang, R. S. Chen, Y. S. Huang, *J. Phys.: Condens. Matter.* **2004**, *16*, 8035.

[90] W. Sugimoto, H. Iwata, Y. Yasunaga, Y. Murakami, Y. Takasu, *Angew. Chem. Int. Ed.* **2003**, *42*, 4092.
[91] K. Fukuda, T. Saida, J. Sato, M. Yonezawa, Y. Takasu, W. Sugimoto, *Inorg. Chem.* **2010**, *49*, 4391.
[92] W. Sugimoto, H. Iwata, Y. Murakami, Y. Takasu, *J. Electrochem. Soc.* **2004**, *151*, A1181.
[93] S. Makino, T. Ban, W. Sugimoto, *J. Electrochem. Soc.* **2015**, *162*, A5001.
[94] W. Sugimoto, K. Yokoshima, K. Ohuchi, Y. Murakami, Y. Takasu, *J. Electrochem. Soc.* **2006**, *153*, A255.
[95] L. Deng, J. Wang, G. Zhu, L. Kang, Z. Hao, Z. Lei, Z. Yang, Z.-H. Liu, *J. Power Sources* **2014**, *248*, 407.
[96] a) Y. Omomo, T. Sasaki, L. Wang, M. Watanabe, *J. Am. Chem. Soc.* **2003**, *125*, 3568; b) Z. Liu, R. Ma, Y. Ebina, K. Takada, T. Sasaki, *Chem. Mater.* **2007**, *19*, 6504.
[97] Z.-h. Liu, K. Ooi, H. Kanoh, W.-p. Tang, T. Tomida, *Langmuir* **2000**, *16*, 4154.
[98] K. Kai, Y. Kobayashi, Y. Yamada, K. Miyazaki, T. Abe, Y. Uchimoto, H. Kageyama, *J. Mater. Chem.* **2012**, *22*, 14691.
[99] K. Kai, Y. Yoshida, H. Kageyama, G. Saito, T. Ishigaki, Y. Furukawa, J. Kawamata, *J. Am. Chem. Soc.* **2008**, *130*, 15938.
[100] C. Xu, S. Shi, Y. Sun, Y. Chen, F. Kang, *Chem. Commun.* **2013**, *49*, 7331.
[101] S. Shi, C. Xu, C. Yang, Y. Chen, J. Liu, F. Kang, *Sci. Rep.* **2013**, *3*, 2598.
[102] J. Coelho, B. Mendoza-Sánchez, H. Pettersson, A. Pokle, E. K. McGuire, E. Long, L. McKeon, A. P. Bell, V. Nicolosi, *2D Materials* **2015**, *2*, 025005.
[103] E. Raymundo-Piñero, V. Khomenko, E. Frackowiak, F. Béguin, *J. Electrochem. Soc.* **2005**, *152*, A229.
[104] J. Zhang, J. Jiang, X. S. Zhao, *J. Phys. Chem. C* **2011**, *115*, 6448.
[105] W. Li, G. Li, J. Sun, R. Zou, K. Xu, Y. Sun, Z. Chen, J. Yang, J. Hu, *Nanoscale* **2013**, *5*, 2901.
[106] J. Liu, J. Jiang, C. Cheng, H. Li, J. Zhang, H. Gong, H. J. Fan, *Adv. Mater.* **2011**, *23*, 2076.
[107] T. Brezesinski, J. Wang, S. H. Tolbert, B. Dunn, *Nat. Mater.* **2010**, *9*, 146.
[108] B. Mendoza-Sánchez, P. S. Grant, *Electrochim. Acta* **2013**, *98*, 294.
[109] D. Hanlon, C. Backes, T. M. Higgins, M. Hughes, A. O'Neill, P. King, N. McEvoy, G. S. Duesberg, B. Mendoza-Sanchez, H. Pettersson, V. Nicolosi, J. N. Coleman, *Chem. Mater.* **2014**, *26*, 1751.
[110] B. Mendoza-Sanchez, D. Hanlon, S. O'Brien, H. Pettersson, J. N. Coleman, V. Nicolosi, *Electrochim. Acta* **2015**, Submitted.
[111] X. Xiao, H. Song, S. Lin, Y. Zhou, X. Zhan, Z. Hu, Q. Zhang, J. Sun, B. Yang, T. Li, L. Jiao, J. Zhou, J. Tang, Y. Gogotsi, *Nat. Commun.* **2016**.
[112] H. Che, A. Liu, *J Mater. Sci-Mater. El.* **2015**, *26*, 4097.
[113] J. Zhou, Y. Huang, X. Cao, B. Ouyang, W. Sun, C. Tan, Y. Zhang, Q. Ma, S. Liang, Q. Yan, H. Zhang, *Nanoscale* **2015**, *7*, 7035.
[114] S. Liu, H. Jia, L. Han, J. Wang, P. Gao, D. Xu, J. Yang, S. Che, *Adv. Mater.* **2012**, *24*, 3201.
[115] J. S. Chen, H. Liu, S. Z. Qiao, X. W. Lou, *J. Mater. Chem.* **2011**, *21*, 5687.
[116] J. Mu, B. Chen, Z. Guo, M. Zhang, Z. Zhang, P. Zhang, C. Shao, Y. Liu, *Nanoscale* **2011**, *3*, 5034.
[117] T. Brousse, D. Bélanger, J. W. Long, *J. Electrochem. Soc.* **2015**, *162*, A5185.
[118] V. Augustyn, P. Simon, B. Dunn, *Energy Environ. Sci.* **2014**, *7*, 1597.
[119] P. Simon, Y. Gogotsi, B. Dunn, *Science* **2014**, *343*, 1210.
[120] J. Zhu, L. Cao, Y. Wu, Y. Gong, Z. Liu, H. E. Hoster, Y. Zhang, S. Zhang, S. Yang, Q. Yan, P. M. Ajayan, R. Vajtai, *Nano Lett.* **2013**, *13*, 5408.
[121] D. H. Nagaraju, Q. Wang, P. Beaujuge, H. N. Alshareef, *J. Mater. Chem. A* **2014**, *2*, 17146.
[122] E. Benavente, M. A. Santa Ana, F. Mendizábal, G. González, *Coord. Chem. Rev.* **2002**, *224*, 87.
[123] G. Eda, H. Yamaguchi, D. Voiry, T. Fujita, M. Chen, M. Chhowalla, *Nano Lett.* **2011**, *11*, 5111.
[124] M. Pumera, Z. Sofer, A. Ambrosi, *J. Mater. Chem. A* **2014**, *2*, 8981.
[125] a) Z. Zeng, Z. Yin, X. Huang, H. Li, Q. He, G. Lu, F. Boey, H. Zhang, *Angew. Chem. Int. Ed.* **2011**, *50*, 11093; b) C. C. Mayorga-Martinez, A. Ambrosi, A. Y. S. Eng, Z. Sofer, M. Pumera, *Electrochem. Commun.* **2015**, *56*, 24.
[126] M. Ghidiu, M. R. Lukatskaya, M.-Q. Zhao, Y. Gogotsi, M. W. Barsoum, *Nature* **2014**, *516*, 78.
[127] M. W. Barsoum, *MAX Phases: Properties of Machinable Ternary Carbides and Nitrides*, Wiley-VCH, Weinheim, Germany **2013**.
[128] a) B. Anasori, Y. Xie, M. Beidaghi, J. Lu, B. C. Hosler, L. Hultman, P. R. C. Kent, Y. Gogotsi, M. W. Barsoum, *ACS Nano* **2015**, *9*, 9507; b) Y. Gogotsi, *Nat. Mater.* **2015**, *14*, 1079.
[129] H.-W. Wang, M. Naguib, K. Page, D. J. Wesolowski, Y. Gogotsi, *Chem. Mater.* **2016**, *28*, 349.
[130] O. Mashtalir, M. Naguib, V. N. Mochalin, Y. Dall'Agnese, M. Heon, M. W. Barsoum, Y. Gogotsi, *Nat. Commun.* **2013**, *4*, 1716.
[131] O. Mashtalir, M. R. Lukatskaya, M.-Q. Zhao, M. W. Barsoum, Y. Gogotsi, *Adv. Mater.* **2015**, *27*, 3501.
[132] M. Naguib, R. R. Unocic, B. L. Armstrong, J. Nanda, *Dalton Transactions* **2015**, *44*, 9353.
[133] M. R. Lukatskaya, S.-M. Bak, X. Yu, X.-Q. Yang, M. W. Barsoum, Y. Gogotsi, *Adv. Energy Mater.* **2015**, 1500589.
[134] Y. Dall'Agnese, M. R. Lukatskaya, K. M. Cook, P.-L. Taberna, Y. Gogotsi, P. Simon, *Electrochem. Commun.* **2014**, *48*, 118.
[135] Y. Dall'Agnese, P.-L. Taberna, Y. Gogotsi, P. Simon, *J. Phys. Chem. Lett* **2015**, *6*, 2305.
[136] Y. Dall'Agnese, P. Rozier, P.-L. Taberna, Y. Gogotsi, P. Simon, *J. Power Sources* **2016**, *306*, 510.
[137] P. Simon, A. Burke, *J. Electrochem. Soc.* **2008**, *17*, 38.
[138] C. Liu, Z. Yu, D. Neff, A. Zhamu, B. Z. Jang, *Nano Lett.* **2010**, *10*, 4863.
[139] W. Gao, N. Singh, L. Song, Z. Liu, A. L. M. Reddy, L. Ci, R. Vajtai, Q. Zhang, B. Wei, P. M. Ajayan, *Nat. Nanotechnol.* **2011**, *6*, 496.
[140] M. F. El-Kady, V. Strong, S. Dubin, R. B. Kaner, *Science* **2012**, *335*, 1326.
[141] M. F. El-Kady, R. B. Kaner, *Nat. Commun.* **2013**, *4*, 1475.
[142] L. Cao, S. Yang, W. Gao, Z. Liu, Y. Gong, L. Ma, G. Shi, S. Lei, Y. Zhang, S. Zhang, R. Vajtai, P. M. Ajayan, *Small* **2013**, *9*, 2905.
[143] J. Feng, X. Sun, C. Wu, L. Peng, C. Lin, S. Hu, J. Yang, Y. Xie, *J. Am. Chem. Soc.* **2011**, *133*, 17832.
[144] B. G. Choi, J. Hong, W. H. Hong, P. T. Hammond, H. Park, *ACS Nano* **2011**, *5*, 7205.
[145] B. Xie, C. Yang, Z. Zhang, P. Zou, Z. Lin, G. Shi, Q. Yang, F. Kang, C.-P. Wong, *ACS Nano* **2015**, *9*, 5636.
[146] J. Qian, H. Jin, B. Chen, M. Lin, W. Lu, W. M. Tang, W. Xiong, L. W. H. Chan, S. P. Lau, J. Yuan, *Angew. Chem. Int. Ed.* **2015**, *54*, 6800.
[147] H. Kang, S. Jung, S. Jeong, G. Kim, K. Lee, *Nat. Commun.* **2015**, 6.
[148] T. Chen, Y. Xue, A. K. Roy, L. Dai, *ACS Nano* **2014**, *8*, 1039.

[149] M.-S. Lee, K. Lee, S.-Y. Kim, H. Lee, J. Park, K.-H. Choi, H.-K. Kim, D.-G. Kim, D.-Y. Lee, S. Nam, J.-U. Park, *Nano Lett.* **2013**, *13*, 2814.
[150] P. Yang, P. Sun, Z. Chai, L. Huang, X. Cai, S. Tan, J. Song, W. Mai, *Angew. Chem. Int. Ed.* **2014**, *53*, 11935.
[151] L. Liang, J. Zhang, Y. Zhou, J. Xie, X. Zhang, M. Guan, B. Pan, Y. Xie, *Sci. Rep.* **2013**, *3*, 1936.
[152] M. Beidaghi, C. Wang, *Adv. Funct. Mater.* **2012**, *22*, 4501.
[153] A. Zhang, C. Wang, Q. Xu, H. Liu, Y. Wang, Y. Xia, *RSC Adv.* **2015**, *5*, 26017.
[154] J. Luo, H. D. Jang, T. Sun, L. Xiao, Z. He, A. P. Katsoulidis, M. G. Kanatzidis, J. M. Gibson, J. Huang, *ACS Nano* **2011**, *5*, 8943.
[155] Y. Xiao, L. Huang, Q. Zhang, S. Xu, Q. Chen, W. Shi, *Appl. Phys. Lett.* **2015**, *107*, 13906.
[156] L. T. Le, M. H. Ervin, H. Qiu, B. E. Fuchs, W. Y. Lee, *Electrochem. Commun.* **2011**, *13*, 355.
[157] B. W. An, K. Kim, M. Kim, S.-Y. Kim, S.-H. Hur, J.-U. Park, *Small* **2015**, *11*, 2263.
[158] H. Jung, C. V. Cheah, N. Jeong, J. Lee, *Appl. Phys. Lett.* **2014**, *105*, 053902.
[159] G. Sun, J. An, C. K. Chua, H. Pang, J. Zhang, P. Chen, *Electrochem. Commun.* **2015**, *51*, 33.
[160] Y. Wang, Y. Shi, C. X. Zhao, J. I. Wong, X. W. Sun, H. Y. Yang, *Nanotechnology* **2014**, 25.
[161] R. Parashkov, E. Becker, T. Riedl, H.-H. Johannes, W. Kowalsky, *Proc. IEEE* **2005**, *93*, 1321.
[162] J. Li, F. Ye, S. Vaziri, M. Muhammed, M. C. Lemme, M. Ostling, *Adv. Mater.* **2013**, *25*, 3985.
[163] C.-L. Lee, C.-H. Chen, C.-W. Chen, *Chem. Eng. J.* **2013**, *230*, 296.
[164] Y. S. Yang, I.-K. You, S.-H. Hong, H.-G. Yun, *ECS Transactions* **2014**, *64*, 135.
[165] S. Bae, H. Kim, Y. Lee, X. Xu, J.-S. Park, Y. Zheng, J. Balakrishnan, T. Lei, H. Ri Kim, Y. I. Song, Y.-J. Kim, K. S. Kim, B. Ozyilmaz, J.-H. Ahn, B. H. Hong, S. Iijima, *Nat. Nanotechnol.* **2010**, *5*, 574.
[166] T. Kobayashi, M. Bando, N. Kimura, K. Shimizu, K. Kadono, N. Umezu, K. Miyahara, S. Hayazaki, S. Nagai, Y. Mizuguchi, Y. Murakami, D. Hobara, *Appl. Phys. Lett.* **2013**, *102*, 023112.
[167] E. S. Polsen, D. Q. McNerny, B. Viswanath, S. W. Pattinson, A. John Hart, *Sci. Rep.* **2015**, *5*, 10257.
[168] X. Yang, C. Cheng, Y. Wang, L. Qiu, D. Li, *Science* **2013**, *341*, 534.
[169] Y. Tao, X. Xie, W. Lv, D.-M. Tang, D. Kong, Z. Huang, H. Nishihara, T. Ishii, B. Li, D. Golberg, F. Kang, T. Kyotani, Q.-H. Yang, *Sci. Rep.* **2013**, *3*, 2975.
[170] C. Lin, X. Zhu, J. Feng, C. Wu, S. Hu, J. Peng, Y. Guo, L. Peng, J. Zhao, J. Huang, J. Yang, Y. Xie, *J. Am. Chem. Soc.* **2013**, *135*, 5144.
[171] J. Lee, S. Lee, G. Li, M. A. Petruska, D. C. Paine, S. Sun, *J. Am. Chem. Soc.* **2012**, *134*, 13410.
[172] Z. Chen, W. Li, R. Li, Y. Zhang, G. Xu, H. Cheng, *Langmuir* **2013**, *29*, 13836.
[173] X. Xie, T. Makaryan, M. Zhao, K. L. Van Aken, Y. Gogotsi, G. Wang, *Adv. Energy Mater.* **2015**, 1502161.
[174] M. A. Lukowski, A. S. Daniel, F. Meng, A. Forticaux, L. Li, S. Jin, *J. Am. Chem. Soc.* **2013**, *135*, 10274.
[175] X. Xiao, C. Zhang, S. Lin, L. Huang, Z. Hu, Y. Cheng, T. Li, W. Qiao, D. Long, Y. Huang, L. Mai, Y. Gogotsi, J. Zhou, *Energy Storage Materials* **2015**, *1*, 1.
[176] K. H. Park, J. Choi, H. J. Kim, D.-H. Oh, J. R. Ahn, S. U. Son, *Small* **2008**, *4*, 945.
[177] a) K. Chang, W. Chen, *Chem. Commun.* **2011**, *47*, 4252; b) K. Chang, W. Chen, *ACS Nano* **2011**, *5*, 4720.
[178] S. Ding, J. S. Chen, X. W. Lou, *Chem. - Eur. J.* **2011**, *17*, 13142.
[179] O. Mashtalir, K. M. Cook, V. N. Mochalin, M. Crowe, M. W. Barsoum, Y. Gogotsi, *J. Mater. Chem. A* **2014**, *2*, 14334.
[180] M. Galiński, A. Lewandowski, I. Stepniak, *Electrochim. Acta* **2006**, *51*, 5567.
[181] B. Mendoza-Sánchez, J. Coelho, A. Pokle, V. Nicolosi, *Electrochim. Acta* **2016**, *192*, 1.
[182] a) Y.-H. Lee, X.-Q. Zhang, W. Zhang, M.-T. Chang, C.-T. Lin, K.-D. Chang, Y.-C. Yu, J. T.-W. Wang, C.-S. Chang, L.-J. Li, T.-W. Lin, *Adv. Mater.* **2012**, *24*, 2320; b) X. Li, C. W. Magnuson, A. Venugopal, R. M. Tromp, J. B. Hannon, E. M. Vogel, L. Colombo, R. S. Ruoff, *J. Am. Chem. Soc.* **2011**, *133*, 2816.
[183] M. Segal, *Nat. Nanotechnol.* **2009**, *4*, 612.
[184] A. Castellanos-Gomez, *J. Phys. Chem. Lett.* **2015**, *6*, 4280.
[185] M. Peplow, *Nature* **2015**, *518*, 17.
[186] W. Auwärter, T. J. Kreutz, T. Greber, J. Osterwalder, *Surf. Sci.* **1999**, *429*, 229.